EVALUATION OF A NOVEL AXIAL FLUX VARIABLE RELUCTANCE MACHINE

A Thesis

presented to the

Faculty of California Polytechnic State University,

San Luis Obispo

In Partial Fulfillment

of the Requirements for the Degree

Master of Science in Electrical Engineering

by

Derek Braden Hines

June 2012

COMMITTEE MEMBERSHIP

TITLE:	Evaluation of a Novel Axial Flux Variable Reluctance Machine
AUTHOR:	Derek Hines
DATE SUBMITTED:	June 2012
COMMITTEE CHAIR:	Dr. Dale Dolan, Assistant Professor
COMMITTEE MEMBER:	Dr. Ahmad Nafisi, Professor
COMMITTEE MEMBER:	Dr. William L. Ahlgren, Associate Professor

ABSTRACT

Evaluation of A Novel Axial Flux Variable Reluctance Machine

Derek Braden Hines

The objective of this thesis is to determine the feasibility of a novel axial flux variable reluctance machine design. The design aims to compete with prevalent rare-earth permanent magnet machines while also implementing an innovative torque ripple minimization strategy. Given the fundamental operating principles, a selection of dimensions, materials, and excitations are prepared for the machine. Special attention is given to the rotor profile which is crucial to operation. Finite element analysis software is used to evaluate a three-dimensional model in terms of inductance and torque. The ultimate potential of the machine is discussed and recommendations for improvement are proposed.

Index terms – Reluctance machine, axial flux, torque ripple, finite element analysis

ACKNOWLEDGEMENTS

My acknowledgements are given to the handful of individuals that have made this culmination of higher education possible. Primarily I owe credit to Newt Ball, whose ingenuity led to the Orbic prototype motor design that forms the core of this thesis. I also praise the efforts of the professors and faculty of the Electrical Engineering Department of Cal Poly, San Luis Obispo. Without them I would not have the theoretical and practical foundation in this discipline. I commend Professor Nafisi for conveying to me Mr. Ball's request for assistance in his design. I also owe credit to my thesis advisor, Professor Dolan, for his guidance. Lastly, I am thankful to my family who are always present to support my endeavors.

TABLE OF CONTENTS

LIST OF TABLES

Table | Page

LIST OF FIGURES

Figure Page

Chapter 1. Introduction

1.1 Background

The origin of this thesis lies in the Orbic prototype motor design of Newton E. Ball in his quest to create an electric machine that employs no permanent magnets. Currently the supply of rare-earth elements utilized for permanent magnets is confined mostly to China. There is concern that increased demand in rare-earth elements will soon cause a shortage of this supply, thus impeding further use of permanent magnet machines. The goal of the Orbic prototype motor design is to satisfy future demands for electric machines without a reliance on rare-earth permanent magnets and ideally to outperform the currently prevalent permanent magnet machines [1]. To meet this end, Mr. Ball has devised a novel axial flux variable reluctance machine (AFVRM).

Variable reluctance machines (VRMs) operate through the tendency of rotor poles to align with the nearest stator poles to minimize magnetic path reluctance, thus producing torque. The stator poles must be excited continually to create a rotating stator flux field for the rotor to follow. Speed of the machine is determined by the frequency of the excitation currents. Sinusoidal excitation is not required for the stator windings as in synchronous or induction machines. Also, the machine is tolerant of faults due to the isolation between stator phase windings. On the rotor there are no windings or permanent magnets for field production. The rotor merely requires the proper geometry, which means there are fewer copper losses and a simple magnetic field behavior. Thus reluctance machines are advantageous due to their simple, robust design. They may

operate at extremely high speeds and produce large torque over many speeds [2], [3]. Their simplicity leads to low manufacturing and maintenance costs [4].

There are a few notable drawbacks to reluctance machines – torque ripple and complex excitation and control. Torque ripple occurs as the rotor moves into alignment with each set of stator poles. Unfortunately, the large variation in inductance required to attain a large torque results in larger torque ripple. Ripple becomes further pronounced at lower speeds and in machines with large step sizes (the rotor displacement from one stator pole to the next). Reducing torque ripple is the most significant challenge to reluctance machine design. Numerous solutions have been proposed in order to minimize torque ripple, either through modification of the machine geometry or through electronic control [4]. Examples include circumferentially displacing the rotors [5] or control of the square of the phase currents using current sensors [6]. The other drawback to VRMs is the inherent complexity of their control. The excitation currents must be applied in a particular manner with regards to rotor position. This ensures the current is applied during decreases of reluctance for motor operation, and vice versa for generator operation. A current drive with rotor position sensors is thus needed. The emergence of power electronics and embedded systems has allowed for the development of small, efficient, practical drives for these machines [7].

In contrast to permanent magnet machines, VRMs can operate at higher speeds, are simpler in structure, and are less costly [5]. The achievable magnetic field of VRMs is stronger and may be controlled unlike permanent magnet machines. However, the power density of VRMs is lower because a higher current density is required for comparable torque [8]. Thus one goal of VRM design is maximizing the power density. This may be

achieved through the axial flux configuration where the primary magnetic flux flow is parallel to the axis of rotation and perpendicular to the face of rotor disks. Axial flux machines are especially valuable in electric vehicles. They are superior to radial flux machines due to a higher power density and greater utilization of lamination material [9]. Greater power density of these machines is possible when the dimensions have a large ratio of diameter to axial length. Increasing the diameter provides greater flux path area [8] for greater torque (torque = force x radius) without altering the axial length [2].

The substantial benefits of axial flux variable reluctance machines make them strong candidates for many applications. The accelerating development and commercialization of electric vehicles, for instance, is stimulating research into reluctance machines for this purpose [2], [3], [9], [8], [5]. Still other uses for VRMs include aerospace and appliance industries [10]. Thus further research and development of variable reluctance machines is a worthwhile undertaking.

1.2 Thesis Scope and Organization

The goal of this thesis is a verification of Mr. Ball's AFVRM design through analysis and simulation. Chapter 2 presents the theory behind the machine design including the method of torque ripple minimization, selection of materials, and selection of dimensions. Chapter 3 encompasses simulations using Ansoft Maxwell, a finite element analysis software created by ANSYS, Inc. It supplies plots of the magnetic field distribution, inductance, core loss, flux linkage, and torque, enabling further refinement of the model. Chapter 4 provides a study of simulation results including a comparison to similar electric machines and suggestions for improvement. Chapter 5 offers the conclusions of this study.

Chapter 2. Design of Novel AFVRM

2.1 Introduction to Design

This novel ARVRM is a high-speed, two-phase motor whose principal feature is the contour of its rotor disks that allow constant torque production. The design consists of axially mounted stator disks layered with rotor disks. Multiple disks are used to minimize the axial force that would occur with only one stator and one rotor disk. They also provide more area for flux and torque production. The complete design calls for six stator disks and five rotor disks, depicted in Figure 2-1. This complete design entails excessive simulation effort, however. Instead, the focus of this study is a two-stator, one-rotor design. The success of this configuration will validate the complete version.

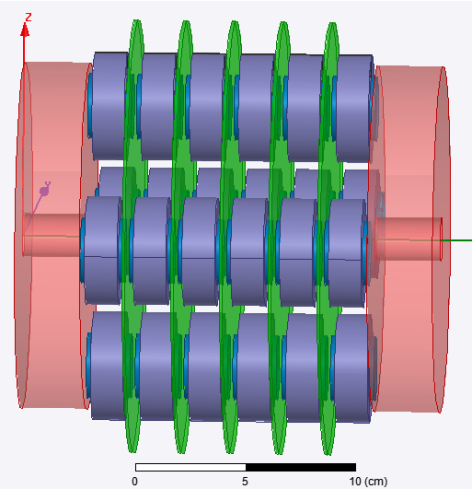

Figure 2-1: Five-rotor, six-stator AFVRM

This machine has four stator poles and two rotor poles (4/2 machine). Each rotor pole encompasses half of the rotor disk, and each pole is divided into four sectors. Figure 2-2 illustrates a face view of the rotor disk. The rotor blades of Sector 1 allow for constant torque production. The formation of these blades is covered in Chapter 3. Sectors 2 through 4 allow for alteration of the excitation current and inductance in preparation for

Sector 1. The small inertia of the rotor derived from its slender profile and large voids make it suitable for high speeds. A lightweight material of low permeability, such as fiberglass, could occupy the voids of the rotor disk. This would reinforce the disk structure and provide heat dissipation.

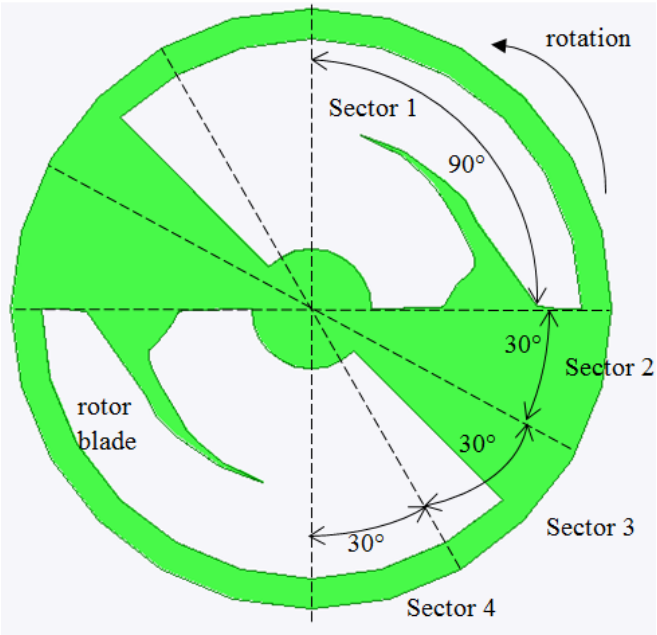

Figure 2-2: Rotor profile

The magnetic circuit (Figure 2-3) is composed of 8 stator poles and 2 end cores at either end of the machine. Stator poles are held in place with magnetically neutral disks. The phase windings are wound around each of the stator poles, a process made easier by the isolation of the stator poles. The cylindrical stator poles allow for the greatest core area per winding length such that copper losses are reduced [1]. There two phases, A and B, separated by 90°.

Reluctance machine designs usually avoid an integer pole ratio because they cause positions of zero torque. This occurs when the rotor poles are either fully unaligned or aligned with the stator poles. With no variation in reluctance, zero torque is produced

and thus the rotor can become stuck. This is avoided in this design from the unique shape of the rotor poles. At the start of torque production, the blade tip will be the nearest portion of the rotor to the excited stator poles and thus will rotate in that direction.

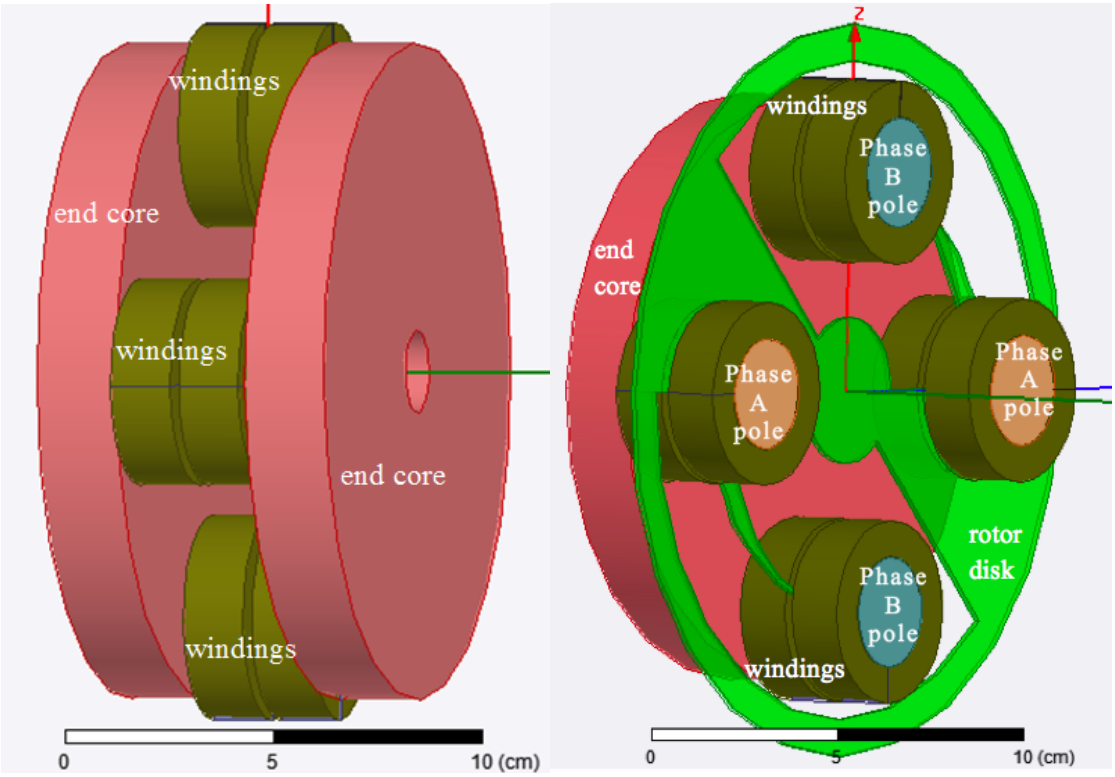

Figure 2-3: Configuration of AFVRM (right end core not shown in right diagram)

2.2 Method of Constant Torque

A remaining drawback to most VRMs is the torque ripple produced as the machine poles alternate between regions of low and high inductance. Often these designs don't specify a particular behavior of inductance during rotation. A constant current is supplied at the appropriate portion of inductance variation; however the ensuing combination results in a torque curve that exhibits ripple. Further design modifications are sometimes made to

correct the problem, such as increasing the number of steps per cycle or using various control strategies.

The unique profile of the rotor blade (Sector 1) aims to solve this issue outright by producing a more specific, complex inductance behavior to generate a constant torque. Furthermore, the rotor design allows for regions of constant inductance between the rotor and stator (Sectors 2 and 4). These regions allow for the non-ideal current rise and fall times that occur from inductance of the phase windings. Ignoring the rise/fall times could limit the speed of the machine or reduce its maximum torque capability [7]. In a motor for instance, a negative torque will result if the current remains during a reduction of inductance, thus subtracting from positive torque production.

The procedure for determining the inductance profile begins with an energy analysis. Flux linkage, energy, and torque with respect to rotor angle θ (radians) are defined as:

$$\lambda = L(\theta) \times i(\theta) \tag{1}$$

$$W = \int_0^{\lambda} i\,(\lambda, \theta)\, d\lambda' \tag{2}$$

$$T = -\frac{\partial W(\lambda, \theta)}{\partial \theta}\bigg|_{\lambda = constant} \tag{3}$$

Assuming linear (non-saturated) operation, the energy and torque equations become

$$W = {}^{1}\!/_{2}\, L(\theta) \times i(\theta)^2 \tag{4}$$

$$T = {}^{1}\!/_{2}\, i^2 \frac{dL(\theta)}{d\theta}\bigg|_{\lambda = constant} \tag{5}$$

Thus, torque arises from the excitation current and the inductance profile of the rotor. A positive steady torque is desired during Sector 1 as the rotor inductance increases,

implying a fall in excitation current. A linear reduction of current is chosen for its simplicity. With a constant torque and chosen current, the inductance behavior can then be derived using (5) as shown in Appendix A. The resulting current (A) and inductance (H) equations are:

$$i(\theta) = -\frac{I_{max}}{2}(\theta - 2) \tag{6}$$

$$L(\theta) = \frac{-L_{max}}{2.33(\theta - 2)} \tag{7}$$

where I_{max} and L_{max} are positive constants defining the maximum current and maximum inductance, respectively. The angle θ has units of radians.

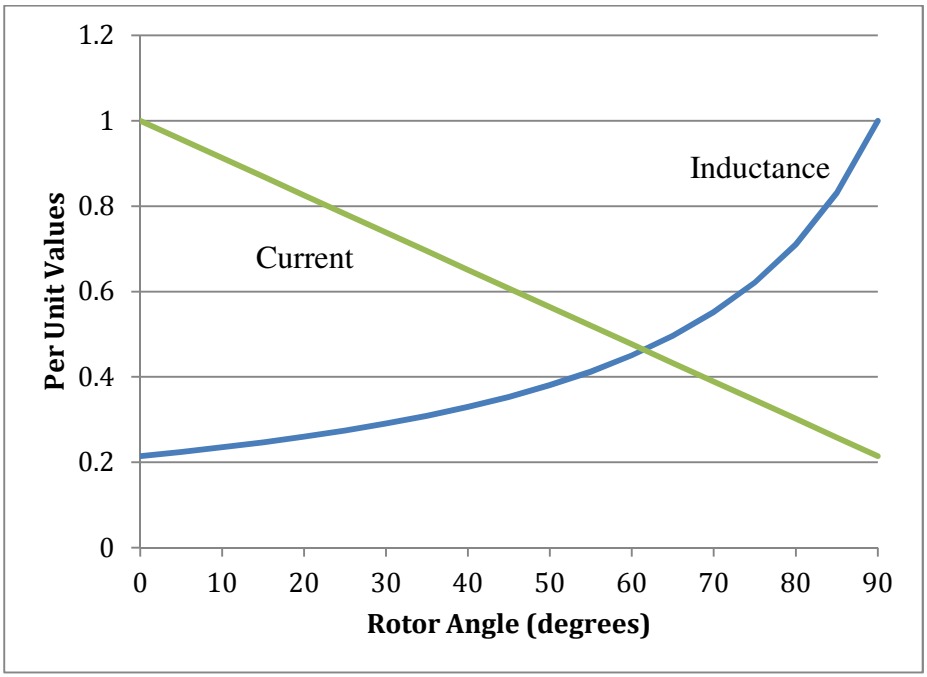

Figure 2-4: Per-unit characteristic curves of inductance and current during Sector 1

Equations (6) and (7) are the characteristic equations for inductance and current serving as estimates for the appropriate behavior. Note from (7) that the nominal L_{max}/L_{min} inductance ratio, α, is fixed to be roughly 4.66. Usually reluctance machines do not have

a predefined ratio that must be followed. In this case however, this condition is imposed with the given current profile and the desire for constant torque.

From equations (6) and (7), the flux linkage (Wb), energy (J), and torque (N-m) during Sector 1 are roughly:

$$\lambda = \frac{I_{max} L_{max}}{4.66} \tag{8}$$

$$W = \frac{-L_{max} {I_{max}}^2 (\theta - 2)}{18.64} \tag{9}$$

$$T = \frac{L_{max} {I_{max}}^2}{18.64} \tag{10}$$

Thus, during Sector 1, the linearly decreasing energy produces a constant torque. Note the constant flux linkage implies that ideally no voltage is induced during this period. Any deviation of the flux linkage from its nominal value, though, will cause some induced voltage in the windings. Also note the magnitudes of flux linkage, energy, and torque are dependent on the maximum values of current and inductance of the machine. These two values are important considerations in the design.

2.3 Machine Behavior through One Rotation

As a reluctance machine, this AFVRM design emphasizes the behavior of the rotor in rotating to alignment with an excited stator pole. The rotor geometry of this design is repeated in Figure 2-5. The machine behavior through an entire cycle may be explained using Figures 2-6 and 2-7.

Beginning at the unaligned position ($\theta = 0°$) is the point of minimum inductance (L_{min}) and the start of Sector 1. Here the stored energy and the excitation current are at their maximum values. From the previous Sector 4, the stator poles have been brought to the

saturation flux density (B_{sat}) of 2 T. The Sector 1 current and inductance profiles mentioned previously allow the operating point to maintain this magnetic field (and constant flux linkage). Operating the machine at 2 T during Sector 1 is already superior to the magnetic field of roughly 0.5 T in permanent magnet machines. For this reason it seems unnecessary to operate the core into saturation as this would create a more complicated analysis.

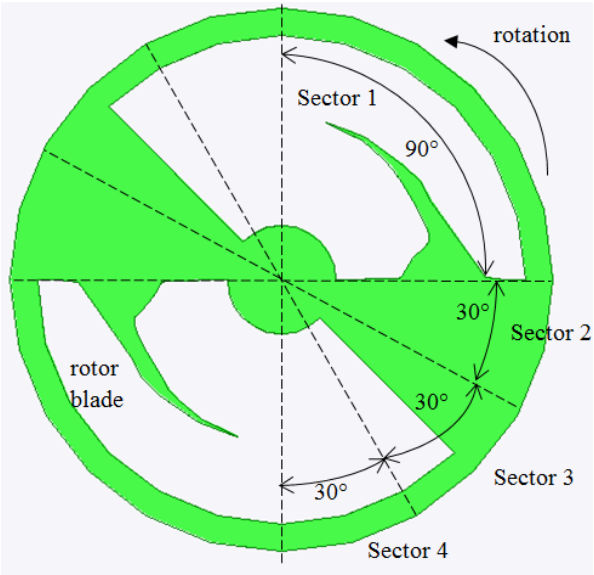

Figure 2-5: Rotor profile (same as Figure 2-2)

During Sector 1 rotation, more rotor area appears between adjacent stator poles until maximum inductance (L_{max}) is obtained at the aligned position ($\theta = 90°$). At this point only the clearance gaps between the stator poles and rotor disk remain. Most of the stored energy has transformed into torque and the current is near its minimum. This rotation, as the reluctance of the flux path decreases, is represented by a series of B-H curves whose slopes (permeability) increase. Stored energy is the area between these curves and the vertical axis, which is seen to decrease during rotation. According to (3),

because flux linkage is constant, the torque is observed to be constant given the intention for linearly decreasing energy through Sector 1.

Sectors 2 to 4 are regions of zero torque. During Sector 2 any remaining excitation current is dropped to zero as the phase inductance discharges. During Sector 3, the rotor voids appear once again and thus inductance decreases until L_{min} is achieved. Current must remain zero or else negative torque will be produced. Finally, during Sector 4, excitation current is returned to its maximum level. Inductance remains at L_{min}, thus resulting in storage of energy to be used during the coming Sector 1 rotation.

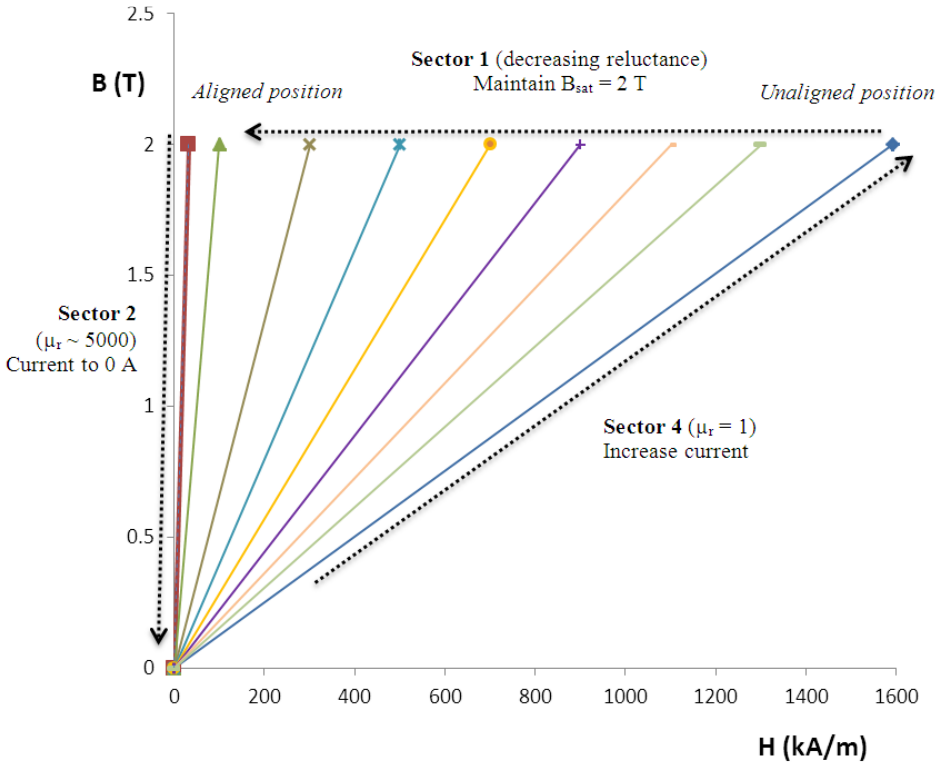

Figure 2-6: Series of B-H curves depicting behavior through rotation of one phase

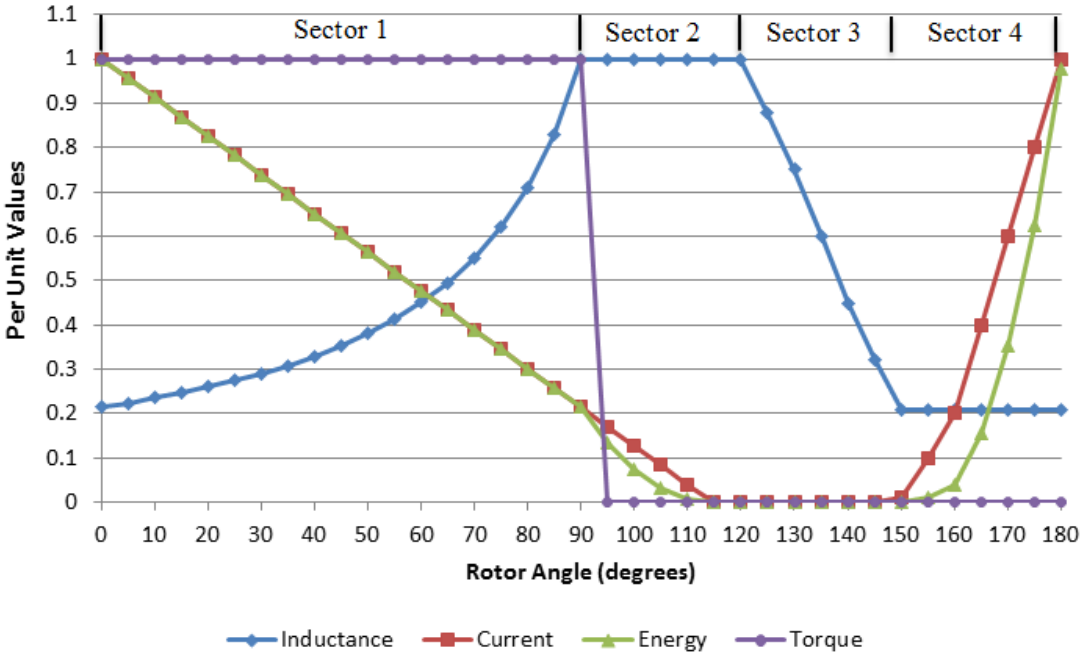

Figure 2-7: Inductance, current, energy, and torque through one rotation (phase A)

2.4 Sizing the AFVRM Design

The envisioned dimension of the complete AFVRM (6 stator disks, 5 rotor disks) is a length and diameter near 20 cm. The length of the one rotor model will be shorter, but the radius can still be 10 cm for the rotor disks. The positions and radii of the stator poles are made so the poles fit suitably over the rotor disk blades. The axial length of the end cores is estimated to provide enough volume for the magnetic field. This volume may be adjusted later using simulation. Figures 2-8 and 2-9 illustrate the initial machine dimensions.

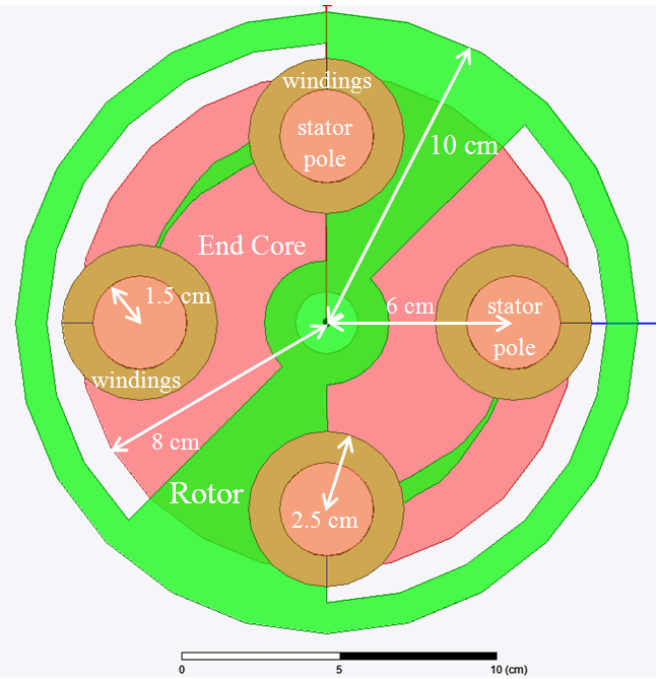

Figure 2-8: Machine dimensions, end view (nearest end core not shown)

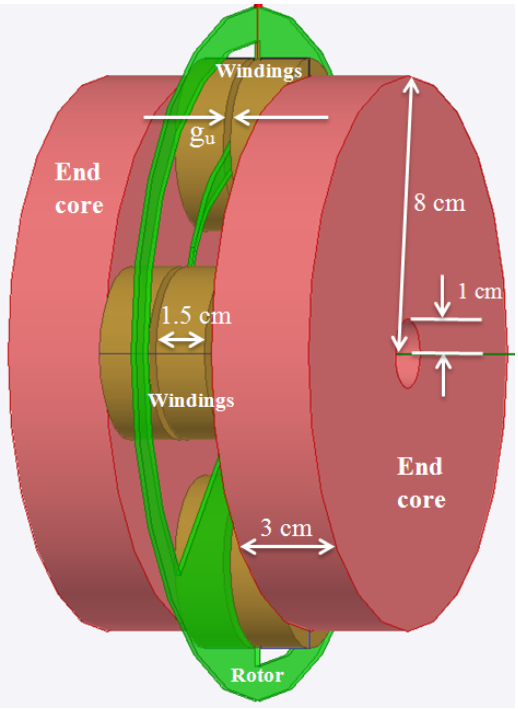

Figure 2-9: Dimensions for magnetic core (stator disks not shown)

Next is the significant task of determining unaligned (minimum) and aligned (maximum) position inductances. In reluctance machine design it is desirable for the inductance ratio α to be high to produce a high torque according to (5). Equation (7) however restrains this ratio to be nearly 4.66, which is already a reasonable value. Further adjustment of torque is possible through the chosen value of L_{max}. For a large L_{max}, a small gap length (clearance between rotor disk and a stator pole) of g_A = 0.015 cm is selected. It is a compromise between achieving a high inductance value versus the feasibility of manufacturing the gap.

Determining the minimum inductance however is not so straightforward. The larger gap length at the unaligned position means that approximations, such as a uniform flux path and neglecting fringing effects, will cause greater discrepancies between nominal and simulated inductance values [7]. Dimensions calculated using the nominal α = 4.66 will thus not give the necessary gap to achieve minimum inductance. Because the goal of the design is to match the characteristic inductance equation, a specific gap ratio, α_g, will be used to size the unaligned gap length. To begin, α_g = 5 is chosen. A series of simulations will be used to obtain the appropriate value. Table 2-1 contains the initial gap values and rotor thickness w_r. Calculations are in Appendix B.

Table 2-1: Initial sizing for gap dimensions

Rotor position	Air Gaps (cm)	α_g	w_r (cm)
Aligned	g_A = 0.015	5	0.12
Unaligned	g_U = 0.15		

Regardless of the value of α_g, other design parameters can be calculated using α = 4.66 with the assurance that the nominal inductance values will result in simulation. The excitation is chosen in order to maintain a saturation flux density of 2 T in the stator core

during Sector 1. The wire gauge and turns per phase of the windings are chosen for a maximum rotor speed of 60,000 rpm and to ensure the maximum current density is below 8 A/mm^2. With the winding excitations determined the stator pole axial lengths and winding dimensions are selected to handle the size of windings around each pole. Tables 2-2 through 2-4 summarize calculated values. Calculations are in Appendix C.

Table 2-2: Calculated magnetomotive force, inductance, and excitation current

Rotor position	MMF (A-turns)	Inductance (mH)	Excitation Current (A)
Aligned	954.93	10.45	11.37
Unaligned	4450	2.24	53

Table 2-3: Values of other design parameters

α	J_{max} (A/mm^2)	Max speed (rpm)	Copper Windings (AWG)	N (turns/phase)	N (turns/stator pole)
4.66	8	60,000	9	84	21

Table 2-4: Dimensions chosen for windings and stator poles

	Radius (cm)		Axial length (cm)
Windings	1.51 (inner)	2.5 (outer)	1.5
Stator Poles	1.5		1.55

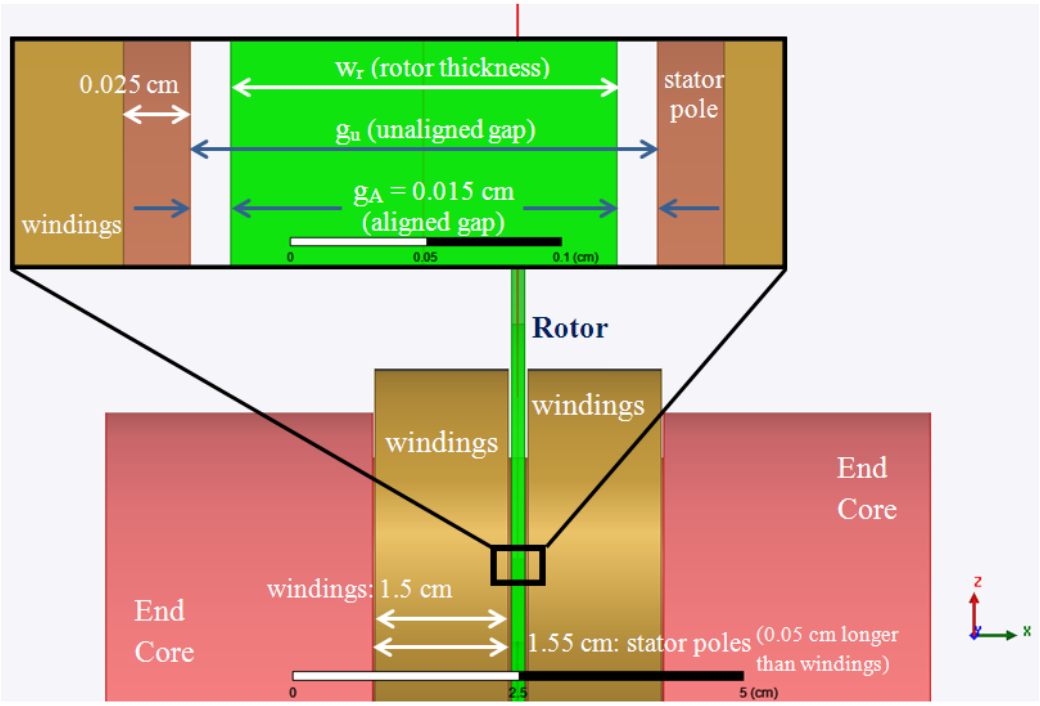

Figure 2-10: Dimensions for gaps and axial lengths, close-up side view

2.5 Materials

The foremost considerations in selecting materials are cost, permeability, and saturation flux density. The torque capabilities of the machine are dependent on the maximum energy storage, which is set by the saturation flux density of the core materials [1]. To certify better performance than machines with rare-earth magnets ($B_{sat} \approx 0.5$ T), a larger saturation flux density is required for the stator poles and end cores. Iron meets the requirement and is also relatively cheap as a soft magnetic alloy.

Since this is a reluctance machine, the other major concern is the selection of a high-permeability material for the rotor disk to maximize the inductance variation for large torque according to (5). Non-grain-orientated (NGO) silicon steel is chosen for its high permeability, relatively low cost, and saturation flux density near that of iron. The more

expensive choice of grain-orientated silicon steel is unnecessary since the direction of magnetic flux will not change during operation. Silicon steel should also be strong enough to handle the rotation of the rotor disks.

Other materials choices include aluminum for the stator disks because it is lightweight, strong, and has permeability near that of air so it is magnetically neutral. Stator windings are simply made of coils of copper wire. Table 2-5 is a summary of the materials, with approximations of the relevant saturation flux density and relative permeability values.

Table 2-5: Summary of materials selected for AFVRM design

Component	Material	
Rotor disks	NGO silicon steel	$\mu_r = 6000$, $B_{sat} = 2.1$ T
Stator disks	aluminum	$\mu_r \approx 1$
Magnetic Core	iron	$\mu_r = 5000$, $B_{sat} = 2$ T
Windings	copper wire	

Chapter 3. Simulation of AFVRM Model

3.1 Introduction to Finite Element Model

The finite element software Ansoft Maxwell is used for verification of the AFVRM design. Finite element analysis (FEA) is a tool that models engineering problems with a finite number of tetrahedral elements. These elements collectively form the mesh. The problem is solved using spatial partial derivative equations with boundary and initial conditions. High accuracy can be obtained through numerous mesh refinements [11].

Ansoft Maxwell will be used to perform a three-dimensional FEA simulation as required by the perpendicular direction of flux with respect to the rotation of the machine's rotor discs. This is further necessitated by the intricate geometry of the rotor blades. Unfortunately, a 3D model entails additional simulation time and complexity. Thus several simplifications are made. Some machine components have little influence on the magnetic field behavior and are thus excluded. These components are the aluminum stator disks, stator windings interconnects, as well as any hardware used to assemble the motor.

The procedure for simulation of the AFVRM model consists of: 1) assembling the model, 2) creation of the rotor blades, 3) verification of magnetic behavior, 4) refinement of dimensions, 5) finalization of rotor blades, and 6) simulation results. The primary model is the simplified two-stator, one-rotor version with associated magnetic core and windings.

3.2 Assembling the AFVRM Model

Simulations utilize the magnetostatic solver type for preparing the final AFVRM model. The geometries of the machine components are made using the initial dimensions as listed in Figures 2-8 to 2-10. Material properties are assigned to the components using material definitions as listed in Table 2-5. These definitions make the assumption of operation in linear magnetic region because this is the intention of the design. Ansoft Maxwell already includes definitions for all the necessary materials except for silicon steel, which must be added.

Once the geometry is defined other considerations are boundary conditions, formation of the mesh, current excitations, and parameter selection. The only boundary condition is the background region defined as a vacuum. This region is required to be 10 times larger than the AFVRM model that it encloses for proper meshing [11]. Ansoft Maxwell automatically creates and refines the mesh according to limits imposed by the user. The adequacy of the generated mesh should be ensured by the user, but generally needs no further improvement as seen through simulations of this model. Current excitations are supplied to the windings. The stranded option is used, which implies a many-stranded conductor with a uniform current density and no eddy and displacement current effects [11]. Finally, the user selects whether inductance and torque is to be measured.

3.3 Creation of the Rotor Blades

To begin, a rough attempt is made at creating the rotor blades. The intent is that as the rotor blades rotate during Sector 1 they shall appear of very narrow width and gradually increase their size until the aligned position. The blade shapes are formed using an assortment of line segments placed by estimation – no sophisticated drawing feature or

mathematical technique is used. The goal is to iteratively refine the shape of the rotor blades until the rotor's inductance versus angle curve closely matches Figure 2-4.

Obtaining the appropriate machine dimensions affects the reluctance, which is not dependent on the machine's excitations. Hence, an arbitrary 400 turns per phase and constant excitation current of 40 A is used to obtain inductance plots. The initial blade design and inductance plot is illustrated in Figure 3-1. Apparently, this initial effort requires much improvement in order to match Figure 2-4.

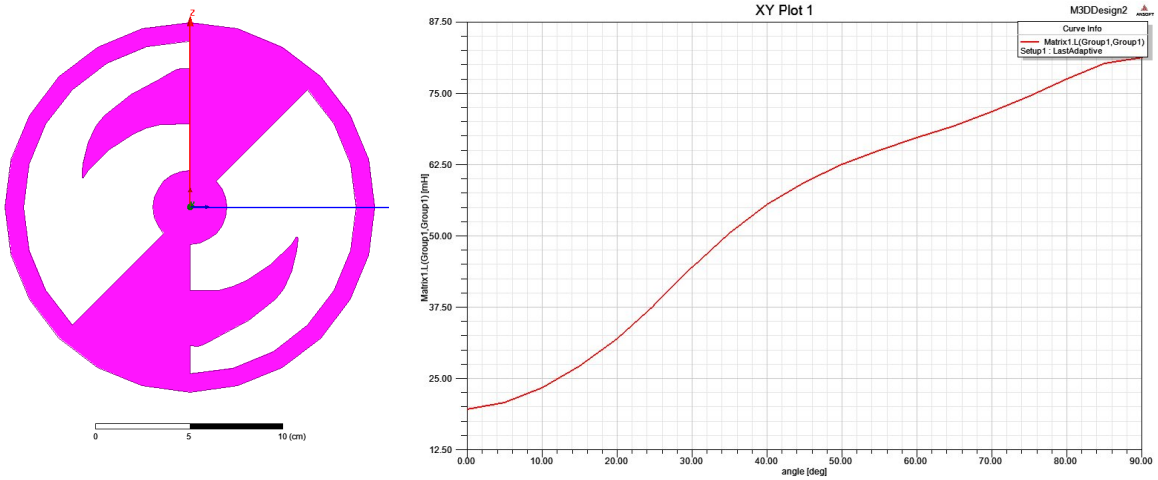

(a) (b)

Figure 3-1: Initial attempt at (a) rotor shape and (b) its inductance vs. angle curve

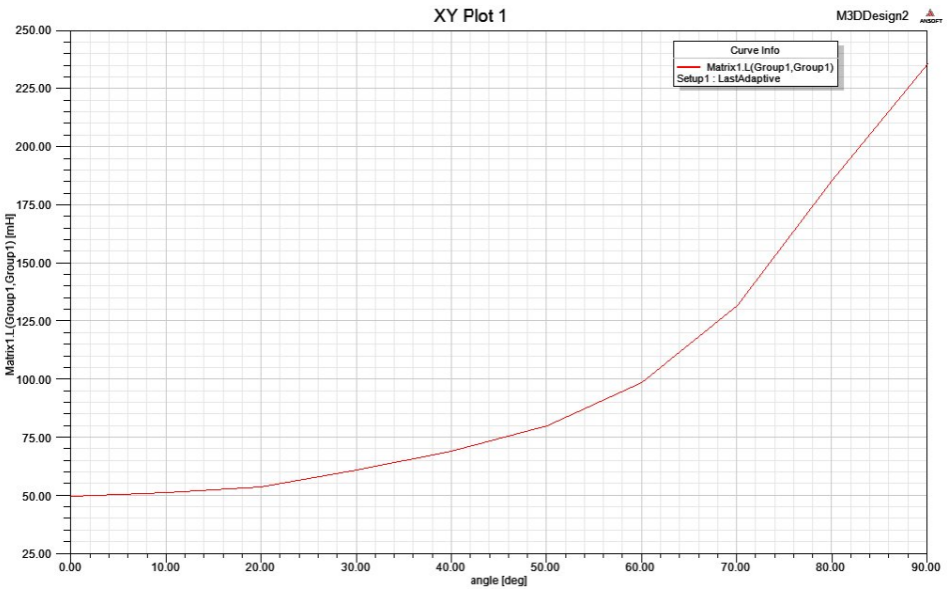

Figure 3-2: Rotor inductance curve after several alterations

After several alterations, the rotor has an inductance curve (Figure 3-2) that better fits the desired shape during Sector 1. Before the final rotor shape can be made the required minimum inductance must be reached through finalizing the air gap dimensions.

3.4 Verification of Magnetic Field Behavior

Further assessment of the initial model is through a verification of the ability of the stator core to conducting magnetic flux. The model with $\alpha_g = 5$ is used with a constant current excitation of 40 A supplied to phase A only. Plots for magnetic field density (B) and magnetic field intensity (H) are taken without and with the rotor present (unaligned and aligned positions).

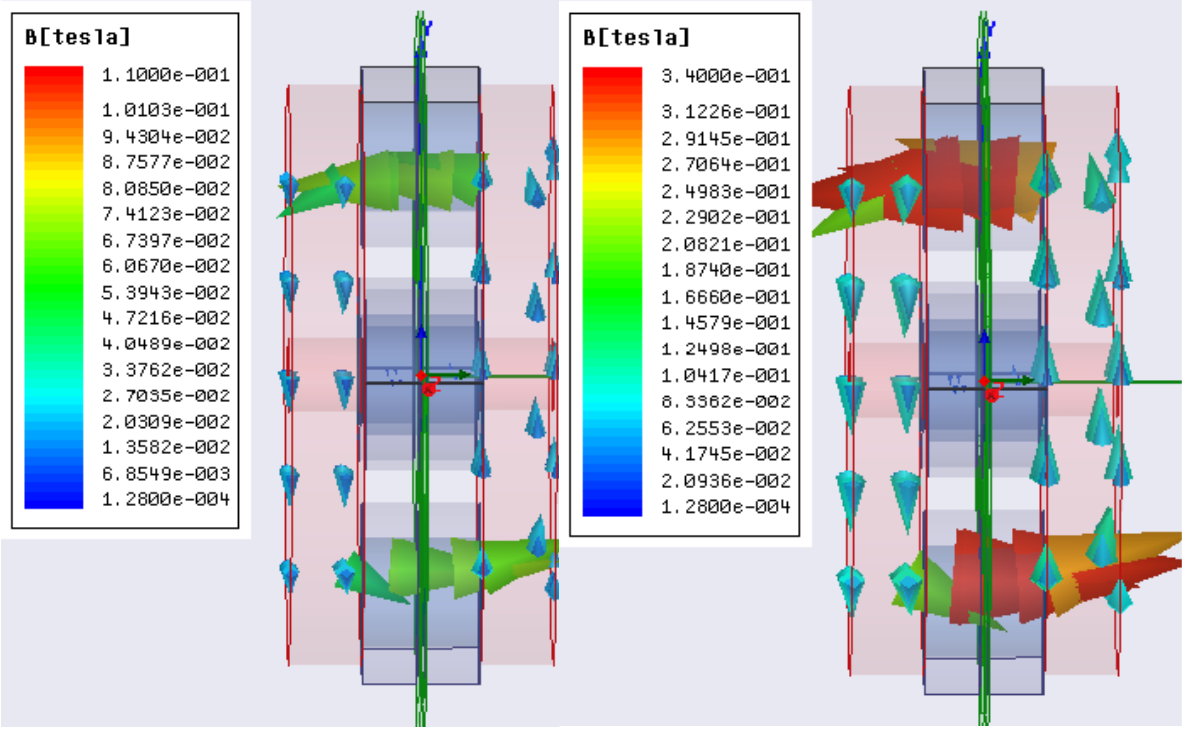

(a) unaligned position (b) aligned position

Figure 3-3: Side view, B field vector plots

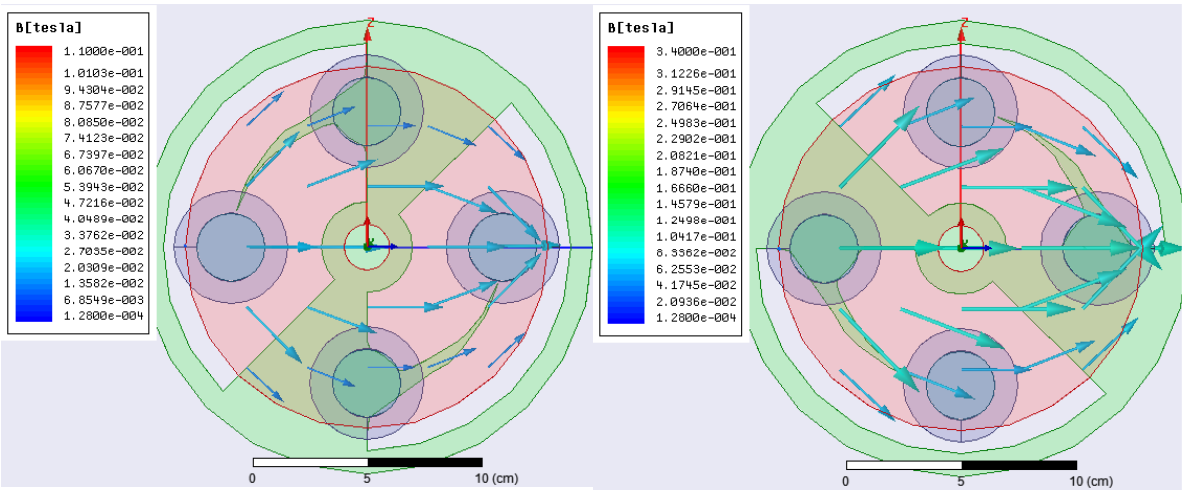

(a) unaligned position (b) aligned position

Figure 3-4: End view, B field vector plots

The direction of the magnetic flux path appears as expected from the direction of current in the excitation windings and the right-hand rule (Figures 3-3 and 3-4). The size of the arrows reveals the flux density is higher through the stator poles than the end cores as the smaller flux path area would suggest. The end view of the machine illustrates the wider distribution of the flux density vectors through the relatively large volume of the end cores. Reduction of the end core volume would be acceptable in order to save weight and size of the complete machine.

The magnitude plots (Figures 3-5 to 3-7) better portray the distribution of the magnetic field. The largest magnitude of the field appears at the edges of the stator poles that touch the end cores. Within the stator poles the field is larger towards the outside and least in the center and against the rotor air gap. Comparing the unaligned and aligned positions shows the desired increase in field strength with the presence of the rotor.

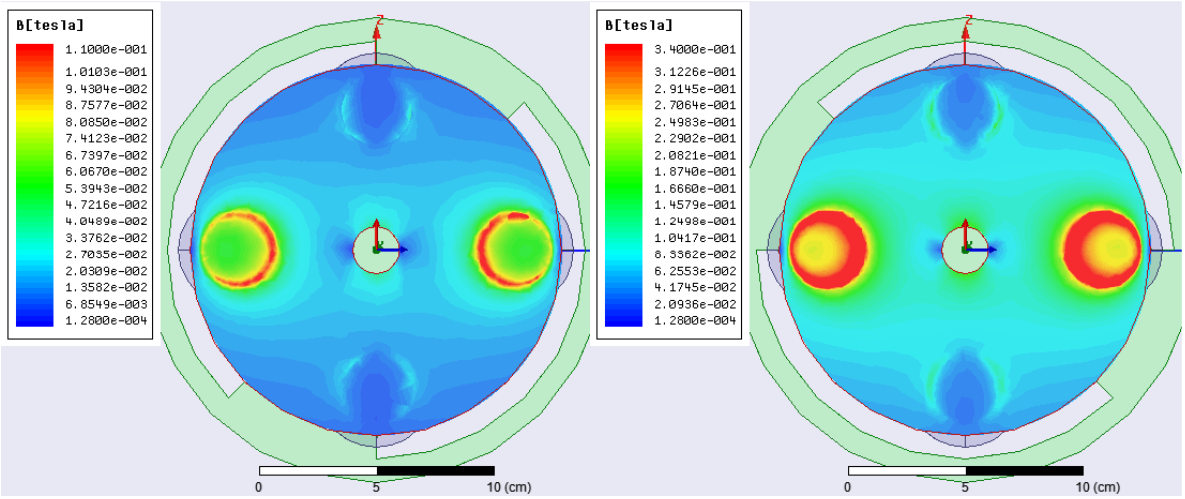

(a) unaligned position (b) aligned position

Figure 3-5: End view, B field magnitude plots

The simulation data values should be checked. The simulation uses a current of 40 A in phase A (4 turns total). The fields displayed in the figures are within the magnetic circuit (μ_r = 5000). Thus, for the aligned position, the magnetic field density (B) and intensity (H) should be roughly:

$$B = \frac{\mu_0 N_{phase} I}{l_{unaligned}} = \frac{4\pi\times10^{-7} H/m \times 4 \times 40\ A}{0.0006\ m} = 0.335\ T \qquad (11)$$

$$H = \frac{B}{\mu_r \mu_0} = \frac{0.335\ T}{5000\times4\pi\times10^{-7} H/m} = 53.33\ A/m \qquad (12)$$

Similarly, for the unaligned position B = 0.067 T and H = 10.67 A/m. These values are in the range of the values displayed in the plots. Hence simulation results are consistent with expectations.

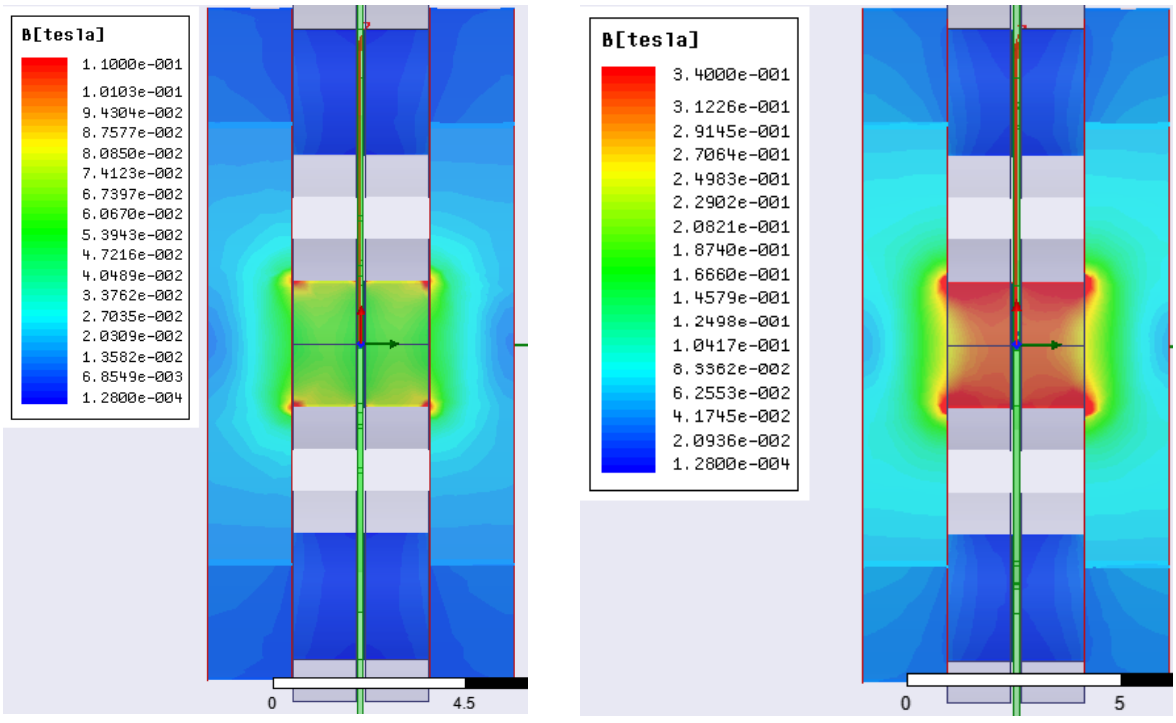

(a) unaligned position (b) aligned position

Figure 3-6: Side view, B field magnitude plots

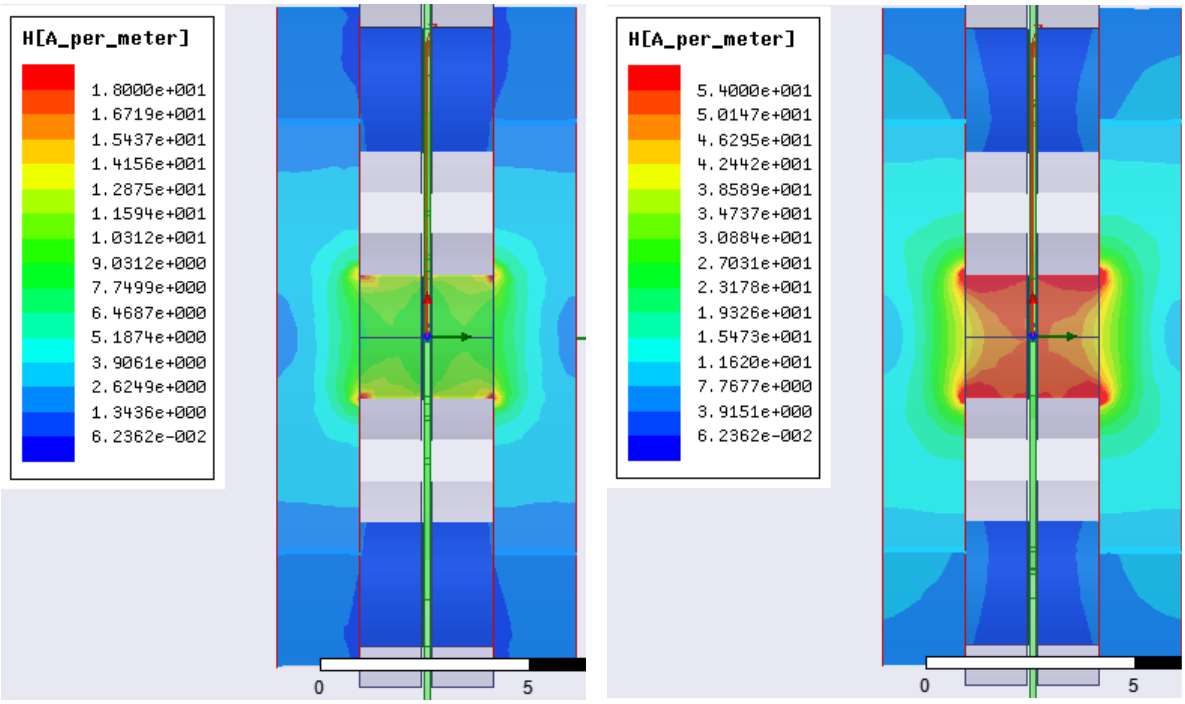

(a) unaligned position (b) aligned position

Figure 3-7: Side view, H field magnitude plots

3.5 Refinement of Machine Dimensions

Before the ultimate rotor shape is made the remaining dimensions are finalized. The proper unaligned gap dimension, $g_{u,}$ is found through performing several simulations until the simulated inductance ratio matches the nominal ratio of 4.66. For this the aligned gap is kept constant (g_A = 0.015cm) while the gap ratio α_g is varied. Table 3-1 summarizes the simulation results using the current rotor shape.

Table 3-1: Obtaining correct gap ratio using simulated inductances

Step	α_g	L_{min} (mH)	L_{max} (mH)	Simulated α
1	5	57.90	234.84	4.06
2	6	49.68	235.85	4.75
3	5.8	50.29	233.51	4.64

These results indicate the gap ratio must be greater than the nominal inductance ratio. The discrepancy occurs from minimum inductance values that are larger than calculated due to a smaller magnetic path reluctance of the unaligned position. This occurs because of the proximity of the rotor blade tip to the stator poles and the presence of the air gap. The result is fringing fields whereby the flux path area is increased such that, in this case, the rotor tip has an influence on the reluctance. Although the inductance ratio is lowered, this behavior is desired because it insures the blade avoids a zero torque scenario at the unaligned position. An inductance ratio of $\alpha_g = 5.8$ results in nearly the desired $\alpha = 4.66$ in simulation and seems suitable for finalizing the dimensions. Table 3-2 has finalized gap dimensions.

Table 3-2: Finalized sizing for gap dimensions

Rotor position	Air Gaps (cm)	α_g	w_r (cm)
Aligned	$g_A = 0.015$	5.8	0.144
Unaligned	$g_U = 0.174$		

One useful feature of the finite element analysis is the observance of the flux distribution through the machine. This may be used, as mentioned previously, to properly size the volume of the end cores. A series of simulations are performed with various axial lengths for the end cores until the magnetic field density within them is greater without exceeding the saturation value of 2 T. The plot for the chosen axial length of 1 cm is in Figure 3-8. The stator poles are at saturation flux density (red region) as expected during Sector 1 operation. Within the end cores the magnitude of the field is nearing 2 T. Thus the reduced volume for the end cores is now better utilized.

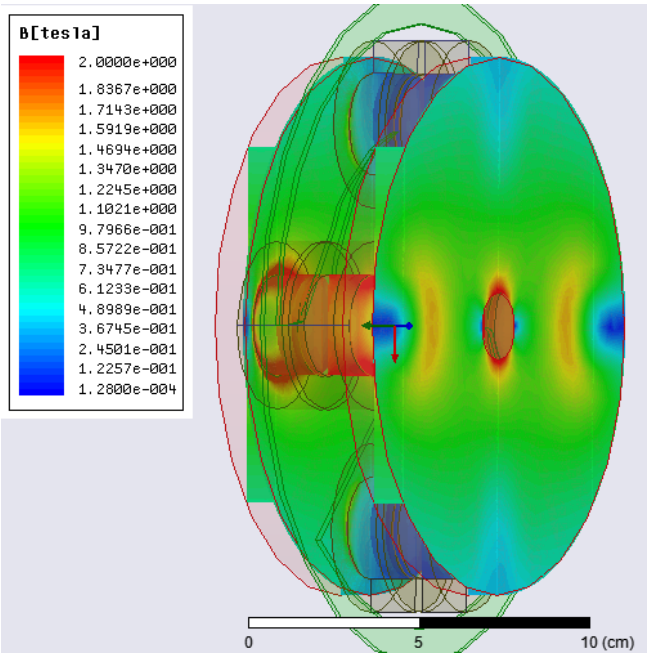

Figure 3-8: Magnetic field density plot for reduction of end core length

3.6 Finalization of Rotor Blades

With the all other machine dimensions determined, the rotor blades may be refined to their final contour. The ultimate purpose of the rotor blades is to allow constant torque production, so properly forming their shape is not a trivial matter. First the blades are created to ensure the maximum and minimum inductance values are achieved. For the maximum inductance, a large blade width at the aligned position is formed so the flux path area will be entirely occupied with rotor material. Then the remaining blade width is adjusted bearing in mind the overlap between rotor positions as it rotates. In other words, the inductance values of adjacent positions are not independent. To maintain simplicity, the simulations compute inductance at every five degrees along the blade. These results are compared to the desired curve and corrections are made (for the remaining rotor alterations the windings have 84 turns as the specified in the design).

The greatest challenge in matching the characteristic inductance curve is achieving the steep rise in inductance as the aligned position is approached ($\theta \sim 80°$). The inductance is too high in this region if the blade is made a smooth sickle shape due to the large blade area at the aligned position. A neck region is created to bring the inductance down for the region $\theta \sim 80°$. This has the unfortunate effect of decreasing inductance of the prior angles ($65° < \theta < 80°$), so then a bulge region is made. Such a process continues towards the tip of the blade, resulting in the blade shape of Figure 3-9, named Rotor 28.

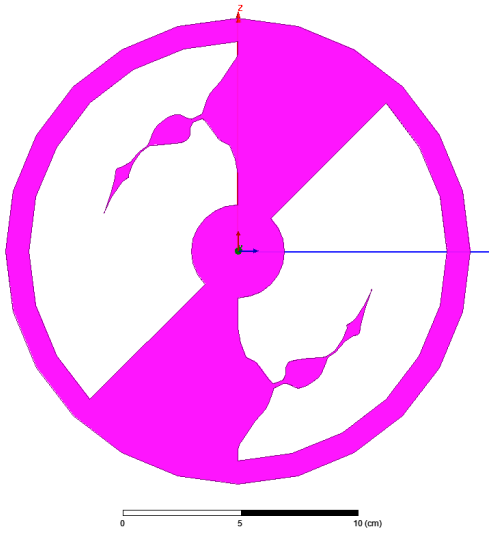

Figure 3-9: Rotor 28 shape

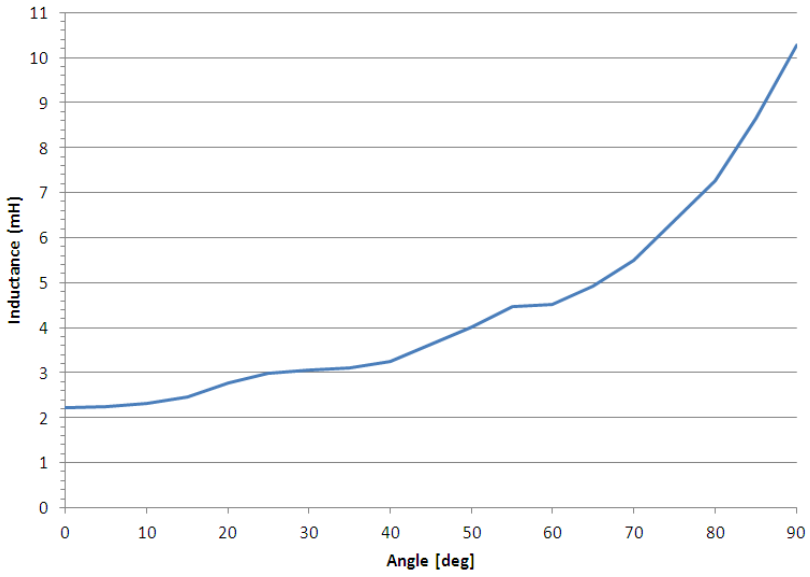

Figure 3-10: Rotor 28 inductance vs. angle curve

This shape gives inductance values that are fairly close to the ideal values. Due to the collection of data at 5 degree steps however, the inductance curve is probably further dissimilar to desired values than depicted. Also, Figure 3-10 reveals that the curve is not agreeably smooth. As the ultimate goal here is to achieve constant torque, torque values at each rotor position may be computed (see Appendix D). The resulting torque ripple is used to determine the suitability of a particular rotor shape. Knowing that ideally the flux linkage is constant, energy and torque may be approximated as:

$$W_n = \frac{1}{2} L_n {I_n}^2 \tag{13}$$

$$T = -\frac{\Delta W(\lambda, \theta)}{\Delta \theta}\bigg|_{\lambda = constant} = -\frac{W_n - W_{n-1}}{\theta_n - \theta_{n-1}} \tag{14}$$

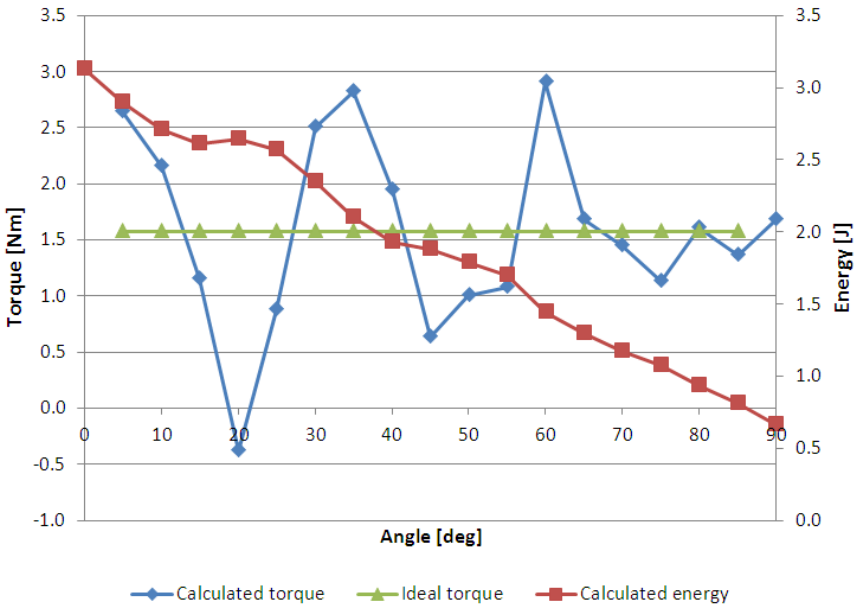

Figure 3-11: Calculated energy and torque from simulated inductances of Rotor 28

For Rotor 28, the torque behavior of Figure 3-11 illustrates that despite the relatively good matching of inductance values, there will be significant torque ripple. The probable reason is the undulating outline of the rotor blade. Instead, the focus is shifted to creating a smooth outline for the rotor blade. This will ensure the energy decreases smoothly such that minimal torque ripple results regardless of how well the inductance curve matches the ideal form. After further efforts, the rotor named Rotor 58 of Figure 3-12 results.

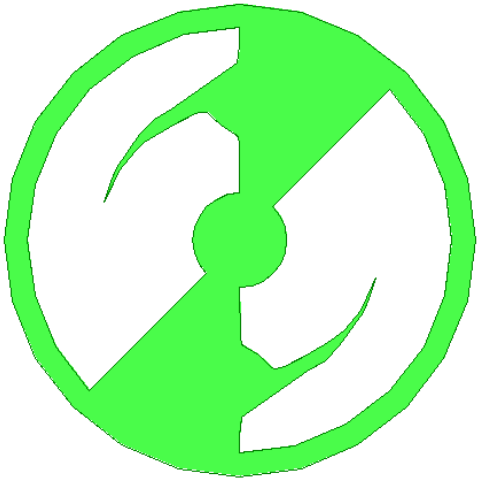

Figure 3-12: Rotor 58 shape

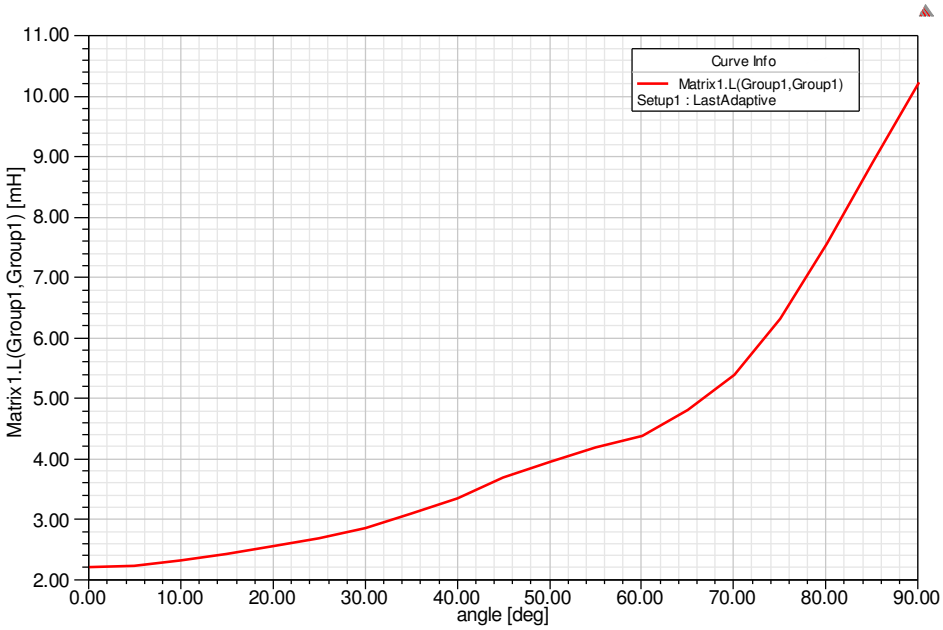

Figure 3-13: Rotor 58 inductance vs. angle curve

The inductance plot of Figure 3-13 demonstrates a smoother curve. The percent error is fairly small with the maximum being nearly 7% (see Appendix D for data). Again, to check the torque ripple, rough torque calculations are performed. A plot of the calculated torque is in Figure 3-14. Still, considerable ripple exists but improvement is seen from the Rotor 28.

After extensive attempts to achieve the desired rotor shape, any more effort is unlikely to be beneficial. Rotor 58 will have to be suitable for the purposes of this study.

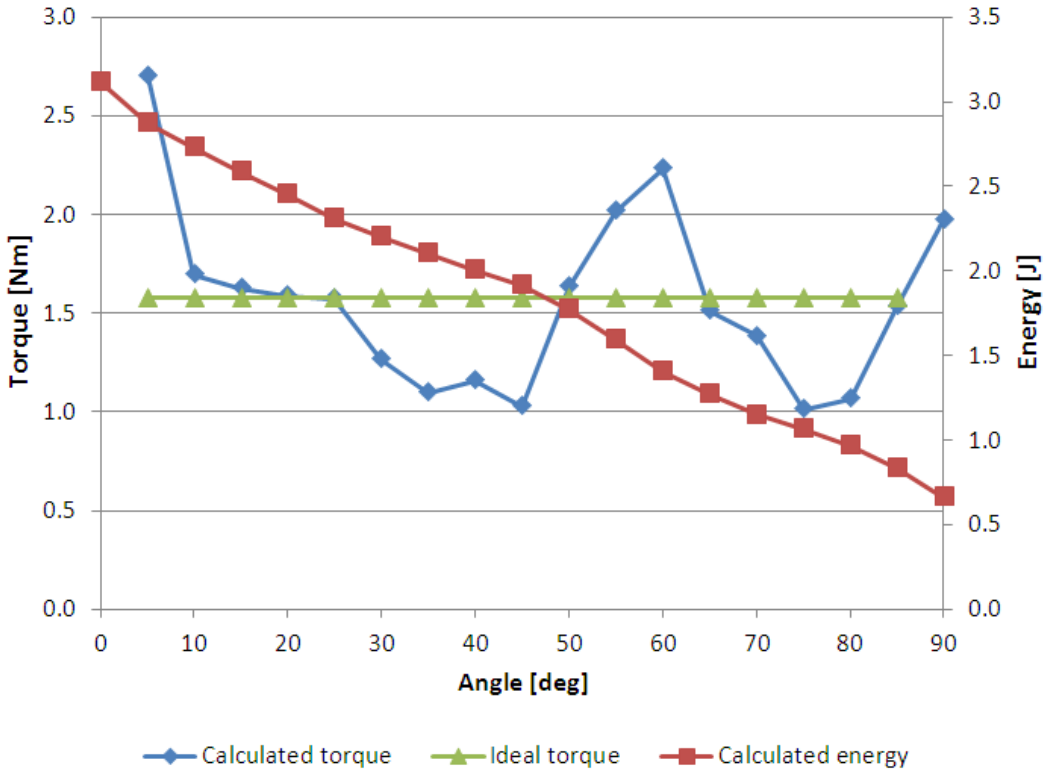

Figure 3-14: Calculated energy and torque from simulated inductances of Rotor 58

3.7 Data Collection for Refined AFVRM Model

With the AFVRM model complete, the performance of the machine may be evaluated through simulation. The transient solver type is necessary for this portion of simulations to best model the variation in current and inductance versus rotor angle and to measure the resulting torque. Measurement of flux linkage, core loss, current, and induced voltage versus time or position will also be possible. The model geometry utilizes Rotor 58, gap dimensions according to $\alpha_g = 5.8$, and the reduced axial length as depicted below.

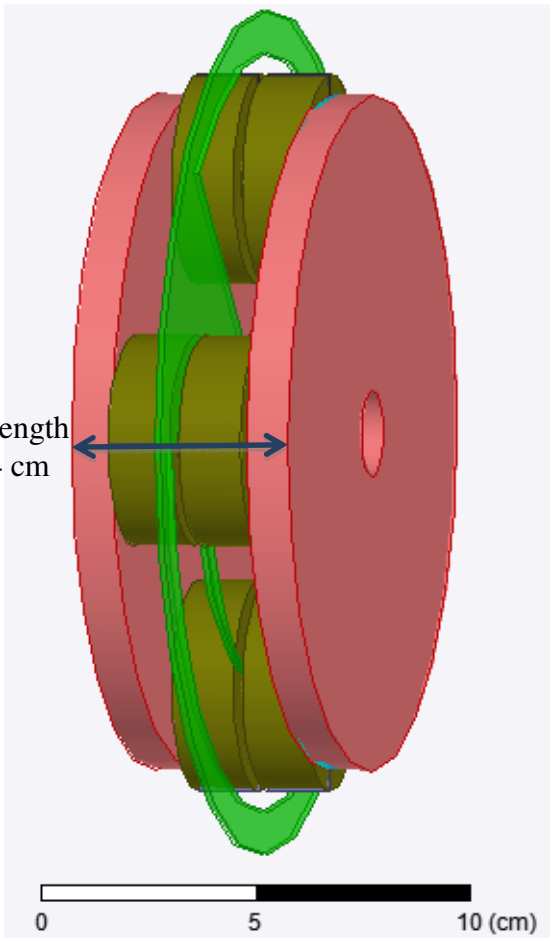

Figure 3-15: Final AFVRM model used in simulations

To model rotation of the rotor disk, motion is added to the simulation. The motion band specifies a special meshing region, including a particular cylindrical gap treatment, which allows for accurate modeling of the rotor's rotation. The especially narrow clearances on either side of the rotor disk (0.015 cm), however, provide exceptional difficulty for Ansoft Maxwell in meshing of this region. Appendix E specifies the details of the motion set-up.

The focus of evaluation will be the behavior during Sector 1 because this is the portion that produces torque. Through the Sectors 2-4 the other excitation phase creates torque. Thus, only phase A will be excited for 90° of rotor rotation. At the end of this 90° the

responsibility of torque production would shift to phase B. The current excitations of the model will no longer be constant but need to follow the characteristic form of (6). The Sector 1 current equation (amps) is modified in terms of time:

$$i(t) = -\frac{I_{max}}{2}\left(\frac{2\pi n_{rotor}}{60}t - 2\right) \tag{15}$$

where n_{rotor} is the rotational speed (rpm) and t = 0 must be the start of Sector 1. This formula allows the excitation current to match the rotor position as would be executed with a position sensor in a real-world machine. Ansoft Maxwell performs units conversions itself, so the equation is entered in the simulation as:

$$i(t) = -\frac{I_{max}}{2}(n_{rotor} \times Time - 2) \tag{16}$$

where "Time" is a reserved intrinsic variable for the time of the transient simulation.

Appropriate parameters are entered in the simulation as summarized in Table 3-4. The maximum current and inductance values found previously are 53 A and 10.45 mH, respectively. Using (8) and (10) the nominal values of flux linkage and torque may be calculated. The imperfect rotor profile will mean that the flux linkage will not be constant. Any deviation from the nominal value will induce voltage in the windings according to $e_{ind} = -N\frac{d\lambda}{dt} = -N\frac{d\lambda}{d\theta}\omega_m$. Thus to minimize the back EMF a speed of 6,000 rpm is selected for simulations. Given this speed, the period required to simulate Sector 1 is given by: $T_{S1} = {}^{15}/_{n_r}$.

Table 3-3: Parameters for simulation and expected flux linkage and torque

I_{max} (A)	N (turns/stator pole)	Rotor speed (rpm)	T_{S1} (ms)	Nominal Flux Linkage (Wb)	Nominal Torque (N-m)
53	21	6,000	2.5	0.119	1.58

The simulation of the one-rotor, two-stator model as specified produces the results of Figures 3-16 through 3-20. The simulation is run with a time step of 0.1 ms, which will give relatively good sampling with 26 data points. Appendix F encompasses data tables of simulated results. Analysis of results follows in Chapter 4.

Figure 3-16 illustrates that the excitation current is following the characteristic form as specified. Thus excitation current will be an unlikely source of any discrepancies in the results.

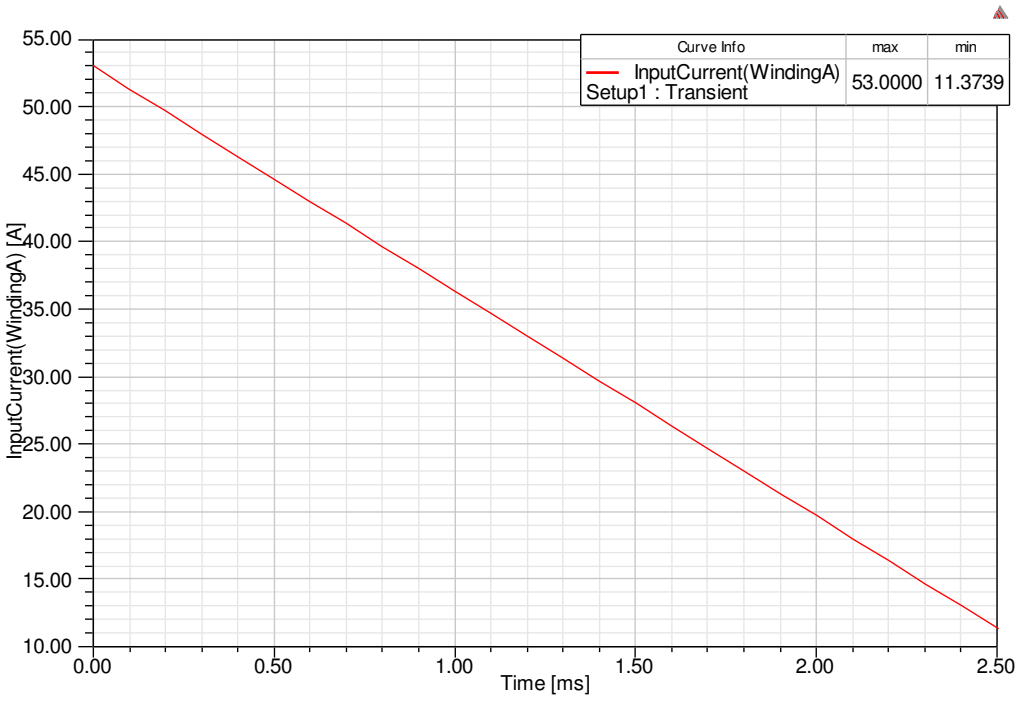

Figure 3-16: Excitation current of Sector 1 (Rotor 58, 6000 rpm, time step 0.1 ms)

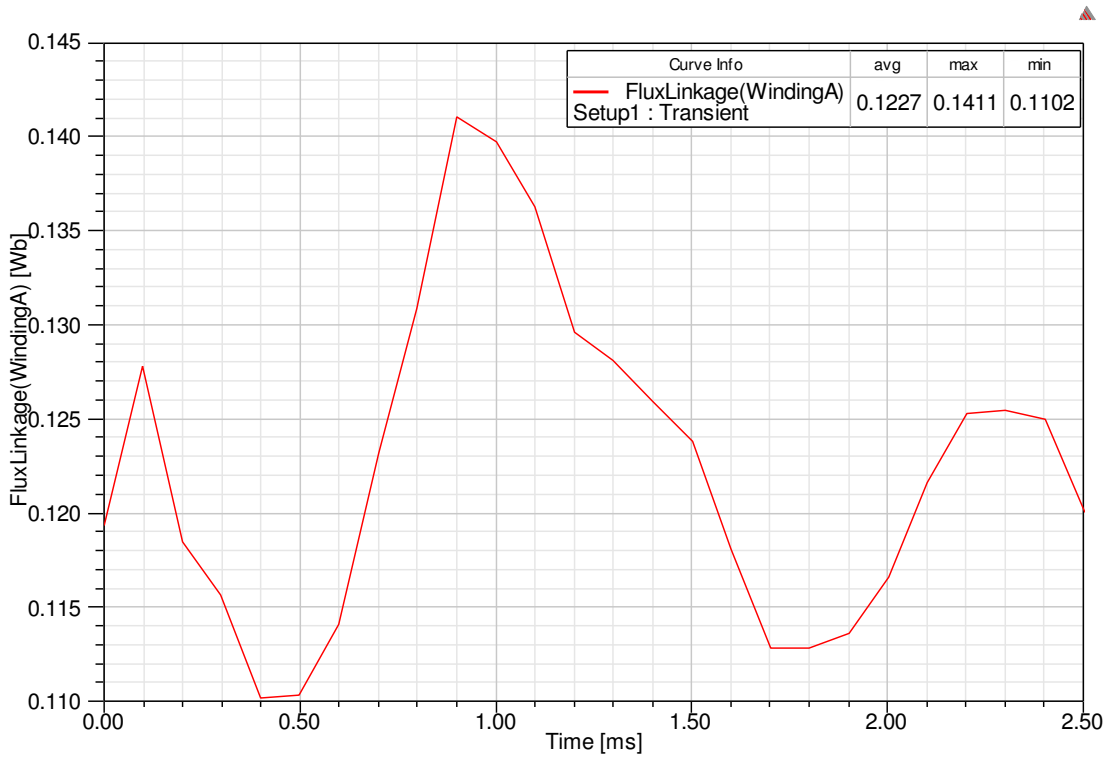

Figure 3-17: Phase A flux linkage of Sector 1 (Rotor 58, 6000 rpm, time step 0.1ms)

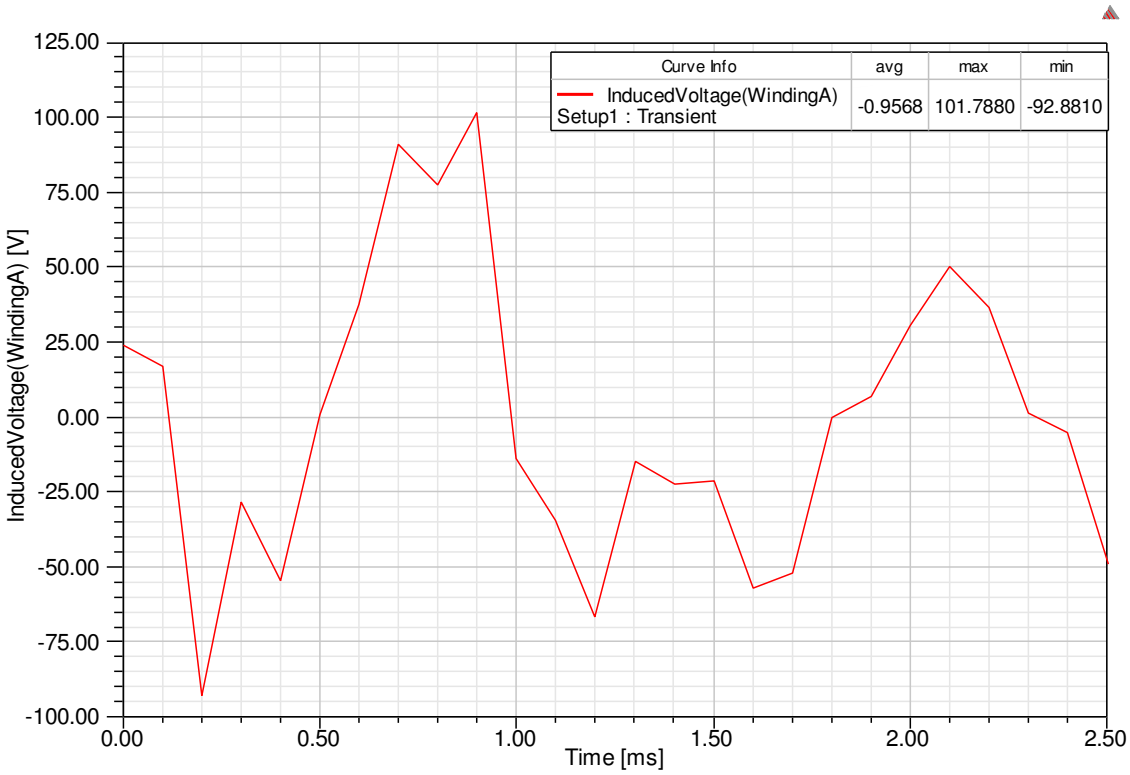

Figure 3-18: Induced Sector 1 phase A voltage (Rotor 58, 6000 rpm, time step 0.1ms)

The behavior of the flux linkage and induced voltage for the phase A windings is depicted in Figures 3-17 and 3-18. Ideally the flux linkage should be constant at 0.119 Wb, and simulation reveals an average of 0.1227 Wb (3.1% error). The induced voltage is desired to be zero, and indeed simulation results in an average of -0.9568 V. Still, the fluctuation of the flux linkage is significant and gives rise to large variations in the induced voltage.

Torque behavior is shown in Figure 3-19, which depicts two measurements of torque performed by the simulation. Recalling the expected constant torque of 1.58 Nm, the average value of the moving torque is fairly close (19% error). The moving torque is the value obtained from motion band. The "torque1.torque" curve however is a more accurate. Initially, this torque exhibits a favorable form, remaining steady at the desired 1.58 Nm. This behavior lasts until 0.8 ms (28.8°), at which point the torque increases significantly. This has the unfortunate effect of making the average torque much greater than its nominal value. Towards the end of Sector 1, the torque has returned to roughly 1.58 Nm as it was initially. Observation of the flux linkage reveals that it too deviates significantly from its ideal value at 0.8 ms.

Finally, a plot of the solid loss and stranded loss is obtained from the simulation (Figure 3-20). The solid loss arise from solid components, in this case the stator core. The fluctuations of this curve are due to the imperfections of the flux behavior of the machine already mentioned. This loss is fairly low and appears desirable. The windings are the source of the stranded loss. The steady reduction in this loss is expected from the decrease in the excitation current of Sector 1. Average simulation values are in Table 3-4.

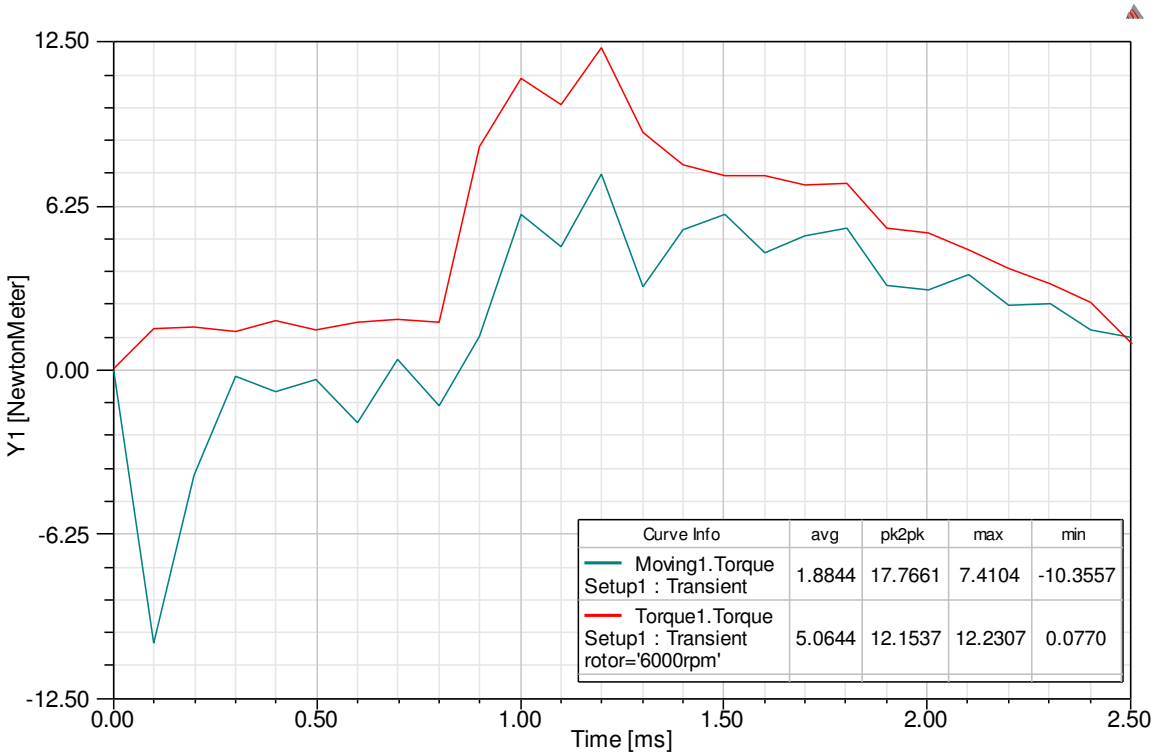

Figure 3-19: Torque of Sector 1 (Rotor 58, 6000 rpm, time step 0.1ms)

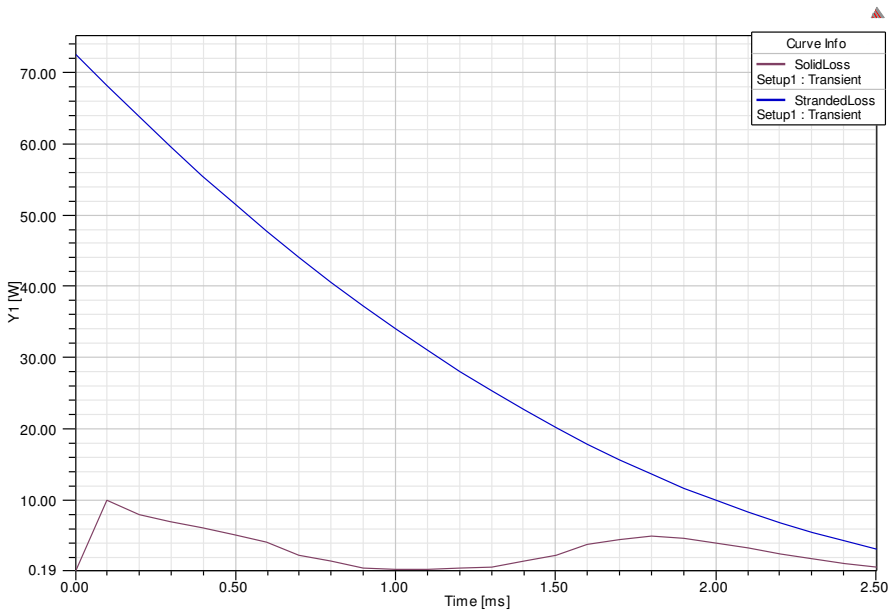

Figure 3-20: Losses of Sector 1 (Rotor 58, 6000 rpm, time step 0.1ms)

Table 3-4: Simulated average values of flux linkage, induced voltage, and torque

Average Flux Linkage	Average Induced Voltage	Average Torque
0.1227 Wb	-0.9568 V	5.0644 N-m

Chapter 4. Analysis of Results

4.1 Interpretation of Results

The objective of this novel AFVRM design is to achieve constant torque production through employing a unique inductance profile. Unfortunately, the simulation results are not entirely encouraging. The source of the discrepancies is derived from the inadequate attempt at achieving the desired inductance form. The favorable torque behavior before 0.8 ms is most likely due to the small width of the rotor blade early into the Sector 1 rotation. The shape in this region is simple and the area is small such that imperfections are not seen. As the rotor blade grows in width, the failure at matching the ideal inductance values becomes apparent and causes the large deviations from ideal behavior. Still, the average flux linkage, average induced voltage, and torque behavior previous to 0.8 ms show there is potential in the design. It seems the rough estimations of torque when forming the rotor profile were an insufficient means of obtaining the desired constant torque behavior.

4.2 Comparison to Other Machine Designs

A primary objective of this design is that it performs comparably, or better, than permanent magnet machines. As a VRM, this machine already has the inherent advantages of lacking permanent magnets and thus has relatively lower cost and greater simplicity. Given the purposes of this study, torque density is a reasonable tool for comparing performance. Several axial flux permanent magnet (AFPM) and axial flux variable reluctance (AFVRM) designs are compared to the novel design of this study in Table 4-1.

Table 4-1: Torque density comparison of several axial-flux machines

	C-Core VRM [10]	Novel AFVRM	In-wheel AFPM [12]	Segmented AFVRM [9]	In-wheel AFPM [13]
Torque (N-m)	~1	5.0644	16.2	28	30
Volume (m^3)	0.4553×10^{-3}	1.657×10^{-3}	4.377×10^{-3}	3.267×10^{-3}	1.787×10^{-3}
Torque Density $\left(Nm/m^3\right)$	2196	3056	3701	8570	16,788

The machine of this study has the second lowest torque density. However, the excessively large average torque from simulation is used for comparison even though the nominal torque is much less. Had the average torque been near the nominal 1.58 Nm, the novel AFVRM would have a much smaller torque density of only 953.5 Nm/m^3. At least in theory, the machine would benefit from having constant torque. As noted in the introduction, a major challenge of variable machine design is matching the torque density capabilities of permanent magnet machines. Indeed, the machine with the greatest torque density has a value 5.5 times that of the machine of this study. VRMs are capable of much greater flux density but at the expense of larger excitations in comparison to permanent magnet machines. For this design, the stator cores and windings had to be large enough in order to achieve a sufficient MMF to reach the operating flux density. This in turn increased the axial length of the machine. Either reducing the machine volume or increasing torque output is required to increase the torque density of this machine.

4.3 Recommendations for Improvement

Currently, the operation of the machine is unacceptable due to the excessive torque ripple. Further development of the rotor blade inductance characteristics is the first

priority in making the performance of the design acceptable. The greatest challenge with the rotor blades is achieving the large inductance increase as the aligned position is approached. This led to the unsuccessful attempt with the undulating outline, known as Rotor 28. One solution to rapidly increasing the inductance could be utilizing several materials for the blade such that permeability rises as rotor angle advances. This option is likely too complex and would not be practical to build. Potentially the most viable solution to matching the inductance characteristic is a variation of the blade contours in three dimensions such that both width and thickness are altered. In any case, a sophisticated program that could relate the inductance to the blade dimensions would be very helpful and ensure the optimum fit to the desired inductance curve.

Although it is possible to refine the present design, perhaps the best approach is to eliminate the complexity of the inductance profile. This is the choice of most other VRM designs, a sensible one given the poor results despite the efforts of this study. Still, a distinctive current and inductance behavior could be envisioned that is innovative over other designs. The excitation current curve could easily possess further complexity through the use of power electronics and controls. A more achievable, simpler inductance profile for the rotor blades could then be found.

Once the preceding issues are addressed such that the machine operates reasonably, the torque density of the machine could be enhanced. For this design another torque equation is derived (Appendix C) to analyze the effects of the various parameters of the machine.

$$T = \frac{\alpha {B_{S1}}^2 A_{core} l_u}{18.64 \mu_0} \quad (17)$$

This form is derived in Appendix C. It reveals how torque production is influenced by the inductance ratio, flux density maintained through Sector 1 (B_{S1}), stator pole cross-sectional area, and the gap between stator poles. For this study, the machine was operated during Sector 1 at the threshold of saturation ($B_{S1} = B_{sat} = 2$ T). Most machine designs, however, specify the machine operate into saturation as it maximizes the energy conversion into torque. Thus, operating at a greater flux density would increase the torque, although this would change the required MMF and so the excitation (current, number of turns, size of windings, etc.) would also need altering.

In order for this machine to compete with the AFPM machine in Table 4-1 of highest torque density, its torque density needs to increase by a factor of 17.6. Some combination of greater torque output and reduced volume is required. If torque output were raised, according to (17), the Sector 1 magnetic flux density would have to be roughly 4.2 times larger than the present 2 T. As the machine is already operating at its saturation threshold, achieving such a great increase in magnetic field is not possible. The other option is reducing the machine volume through compacting its configuration. VRMs are dependent on their volume for supplying excitation to create sufficient MMF. In the present design the required flux production determines the axial length of the stator cores and hence that of the entire machine. Furthermore, the volume of the end cores is not efficiently utilized as seen by the flux path of phase A and phase B. An appealing solution is to maintain the rotor disk concept of this design but replace its stator core with the c-core topology developed in [2] and [3], and similar to [10]. This configuration

provides greater surface area for the windings, is more compact, and requires no massive end cores. To reach a torque density near 16,788 N-m/m^3, the present volume of $1.657x10^{-3}$ m^3 would need to be reduced by a factor of 17.6. Such a reduction is unlikely. In considering a combination of both torque output and volume enhancements, it seems implausible for this AFVRM to reach the superior torque density of the best PM machines.

Chapter 5. Conclusions

Through theoretical analysis and simulation results of the novel AFVRM proposed, this study reveals that substantial further development is necessary for acceptable performance. The principal flaw of the design is its complexity. In the realm of the design's theory, the concept of constant torque behavior is appealing and appears to work according to calculations. In reality, the simulations reveal how any small deviation from the characteristic inductance of the blades will generate excessive torque ripple. The inherent complexity of the rotor blades makes the usefulness of this design poor until these issues are resolved. The best option may be to revise the design to transfer complexity to the excitation current, thus enabling a simpler inductance profile. Still, the torque density of this design is poor relative to other machines. Despite possible enhancements, it is unlikely that its torque density will ever be competitive with permanent magnet machines. However, with suitable development of the inductance characteristics, it seems plausible for the machine to achieve acceptable if not excellent constant torque operation. This is a notable advantage of this design in conjunction with it comparable low cost and the growing concern of the future of rare-earth element resources. With proper refinement, such advantages of this novel AFVRM may give it widespread use as the favored alternative to permanent magnet machines.

BIBLIOGRAPHY

[1] N.E. Ball. (2011, March 16). *Motor Story*, [Online]. Available: http://www.orbicinstitute.org/motor_story.html

[2] A. Labak and N.C. Kar, "A novel five-phase pancake shaped switched reluctance motor for hybrid electric vehicles," in *Proc. IEEE Vehicle Power and Propulsion Conference*, VPPC '09. pp.494-499.

[3] A. Labak and N.C. Kar, "Development and analysis of a five-phase pancake shaped switched reluctance motor," presented at the *XIX International Conference on Electric Machines*, Rome, 2010.

[4] F. Daldaban and N. Ustkoyuncu, "Multi-layer switched reluctance motor to reduce torque ripple," *Energy Conversion and Management*, vol. 49, issue 5, pp.974-979, 2008.

[5] R. Madhavan and B.G. Fernandes, "A novel technique for minimizing torque ripple in axial flux segmented rotor SRM," presented at the *Energy Conversion Congress and Exposition*, Phoenix, AZ, 2011.

[6] N. Inanc, "Phase current modulation of switched reluctance motor to minimize torque ripple," *Electric Power Systems Research*, vol. 61, issue 1, pp.51-55, 28 Feb. 2002.

[7] A.E. Fitzgerald, C. Kingsley Jr., S.D. Umans, "Variable-Reluctance Machines and Stepping Motors," in *Electric Machinery*, 6th ed. New York: McGraw-Hill, 2003.

[8] H. Arihara and K. Akatsu, "Characteristics of axial type switched reluctance motor," presented at the *Energy Conversion Congress and Exposition*, Phoenix, AZ, 2011.

[9] R. Madhavan and B.G. Fernandes, "A novel axial flux segmented SRM for electric vehicle application," presented at the *XIX International Conference on Electric Machines*, Rome, 2010.

[10] S.H. Mao and M.C. Tsai, "A novel switched reluctance motor with C-core stators," *IEEE Trans. Magnetics*, vol. 41, no. 12, pp. 4413-4420, Dec. 2005.

[11] "Maxwell 3-D Technical Notes," Ansoft Maxwell, Version 14.0.2, Ansys, Inc.

[12] H. Lovatt, V. Ramsden, B. Mecrow, "Design of an in-wheel motor for a solar-powered electric vehicle," IEE Proc. Elect. Power Appl., vol. 145, pp.402-408, Sept. 1998.

[13] F. Caricchi, F. Crescimbini, E. Fedeli, G. Noia, "Design and construction of a wheel-directly-coupled axial-flux PM motor prototype for EVs," *Industry Applications Society Annual Meeting, 1994., Conference Record of the 1994 IEEE* , vol. 1, pp.254-261, 2-6 Oct 1994.

Appendix A. Derivation of Sector 1 Current and Inductance Equations

These formulas are approximations of the desired current and inductance behaviors versus rotor angle in radians during Sector 1. To begin, linear operation is assumed and per unit values are used. The current is chosen to follow the form:

$$i(\theta) = -\frac{I_{max}}{2}(\theta - 2)$$

This will give about 80% reduction in I_{max} during Sector 1 rotation. This means there will be 20% left of the current to decay in Sector 2. A constant torque is desired (A and C are constants), so the inductance equation may be derived as follows:

$$T = {}^{1}\!/_{2}\, i^2 \frac{dL(\theta)}{d\theta}\bigg|_{\lambda=constant} = A$$

$$T = {}^{1}\!/_{2}\left(-\frac{I_{max}}{2}(\theta - 2)\right)^2 \frac{dL(\theta)}{d\theta} = A$$

$$T = \frac{{I_{max}}^2}{8}(\theta - 2)^2 \frac{dL(\theta)}{d\theta} = A$$

$$\int L(\theta) = \int \frac{8A}{{I_{max}}^2(\theta - 2)^2}\, d\theta = \int \frac{C}{(\theta - 2)^2}\, d\theta$$

$$L(\theta) = \frac{-C}{(\theta - 2)}$$

This equation needs to be set so $L(\pi/2) = L_{max}$.

$$L(\pi/2) = \frac{-C}{(\pi/2 - 2)} = L_{max}$$

$$C = -L_{max}(\pi/2 - 2) = \frac{-L_{max}}{2.33}$$

Substituting C back into L(θ) gives:

$$L(\theta) = \frac{-L_{max}}{2.33(\theta - 2)}$$

Appendix B. Calculations for Machine Design Gap Lengths

These calculations are for the initial gap dimensions with the initial value of $\alpha_g = 5$. The aligned gap is $g_a = 0.015$ cm. In calculating the gap lengths given the inductance ratio, the unaligned gap is found by:

$$g_u = 2 \times \alpha \times g_a$$

This is because between a set of stator poles there are two aligned gaps and one unaligned gap.

$$g_u = 2 \times 5 \times 0.015cm = 0.15\ cm$$

Also, the width of the rotor is: $w_r = 0.15\ cm - 2 \times 0.015 = 0.12\ cm$.

Appendix C. Calculations for Machine Parameters

Remaining design parameters are found using α = 4.66. The gap lengths will not actually be used in the simulated design but represent the equivalent gap lengths under assumptions such as uniform path length, no fringing, uniform core cross-sectional area, etc. Also the relatively small reluctances of the stator and rotor are neglected. Note subscripts: "u" – unaligned, "a" – aligned.

1. Unaligned gap: g_u = 0.1398 cm (found as in Appendix B).
2. Total air gap lengths, with two such gaps between aligned rotor and stator pole.

$$l_a = 2 \times 2\ gaps \times 0.015 cm/gap = \ 0.0006\ m$$

With g_U = 0.1398 cm between stator poles, the total unaligned gap is:

$$l_u = 2\ gaps \times 0.1398 cm/gap = \ 0.002796\ m$$

To check, $\alpha = \frac{L_{max}}{L_{min}} = \frac{l_u}{l_a} = \frac{0.002796\ m}{0.0006\ m} = 4.66.$

3. Magnetomotive force (MMF) to maintain B_{sat} = 2 T in stator poles.

$$\mathcal{F}_a = H_{sat} \times l_a = \frac{B_{sat} \times l_a}{\mu_0} = \frac{2\ T \times 0.0006\ m}{4\pi \times 10^{-7} H/m}$$

$$\mathcal{F}_a = 954.93\ A - turns$$

$$\mathcal{F}_u = \alpha \mathcal{F}_a = 4.66 \times 954.93 = 4450\ A - turns$$

4. Maximum frequency of rotor current given maximum rotor speed of 60,000 rpm and 2 rotor poles, P_r.

$$f_{s,max} = \frac{n_{rotor} P_r}{60} = \frac{60{,}000 rpm \times 2}{60 sec/min} = 2000\ Hz$$

5. Choose wire gauge. Using as AWG conductor chart, choose a wire to have 100% skin depth up to 2000 Hz.

Table C-1: Specifications for chosen wire gauge

AWG	Diameter	A_w, cross-sectional area	Resistance	f_{max}, for 100% skin depth
9	2.90576 mm	6.63 mm^2	2.598 Ω/km	2050 Hz

6. Find number of turns per stator phase. The unaligned MMF is used because this position requires the most current to maintain B_{sat}. Aim to keep current density below 8 A/mm^2.

$$N_{phase} \geq \frac{\mathcal{F}_u}{A_w J_{max}} = \frac{4450\ A - turns}{6.63 mm^2 \times 8 \frac{A}{mm^2}} = 83.9\ turns$$

$$N_{phase} = 84\ turns$$

There are 4 stator poles per phase, so per pole there are N_{pole} = 21 turns.

7. Excitation current to maintain B_{sat} through Sector 1.

$$I_a = \frac{\mathcal{F}_a}{N_{phase}} = \frac{954.93\ A - turns}{84\ turns} = 11.37\ A$$

$$I_{max} = I_u = \frac{\mathcal{F}_u}{N_{phase}} = \frac{4450\ A - turns}{84\ turns} = 53\ A$$

8. Inductance values. Cross-sectional area of the magnetic circuit is approximated as the area of the stator poles, A_{core}.

$$A_{core} = \pi \times (0.015\ m)^2 = 0.0007069\ m^2$$

$$L_{max} = \frac{{N_{phase}}^2}{\Re} = \frac{\mu_0 A_{core} {N_{phase}}^2}{l_a} = \frac{4\pi \times 10^{-7} H/m \times 0.0007069\, m^2 \times\ 84^2}{0.0006\, m}$$

$$L_{max} = 10.45\, mH$$

$$L_{min} = \frac{L_{max}}{\propto_n} = \frac{10.45\, mH}{4.66} = 2.24\, mH$$

9. Required dimensions of windings and axial length of stator poles to hold these windings. Needed cross-sectional area of windings:

$$A_c = N_{pole} \times A_w = 21 \times 6.63 mm^2 = 139.23\, mm^2$$

Dimensions are chosen as follows where the stator pole radius 1.5 cm is already chosen. Note the small clearance between poles and windings.

Table C-2: Dimensions chosen for windings and stator poles

	Radius (cm)		Axial length (cm)
Windings	1.51 (inner)	2.5 (outer)	1.5
Stator Poles	1.5		1.55

Thus the windings provide an area of:

$$A_c = (r_{out} - r_{in}) length = (25mm - 15.1mm) \times 15mm$$

$$A_c = 148.5\, mm^2$$

This is greater than the required 139.23 mm^2. Check the current density is below maximum of 8 A/mm^2.

$$J = \frac{NI}{A} = \frac{21\ turns \times 53\ A}{148.5\, mm^2} = 7.495\ A/mm^2$$

Using some of the design equations and (10) one may obtain the torque equation (discussion in Chapter 4):

$$\mathrm{T} = \frac{L_{max} {I_{max}}^2}{18.64} = \frac{\left(\frac{\mu_0 A_{core} {N_{phase}}^2}{l_a}\right)\left(\alpha \frac{B_{S1} \times l_a}{N_{phase} \mu_0}\right)^2}{18.64} = \frac{\alpha^2 {B_{S1}}^2 A_{core} l_a}{18.64 \mu_0}$$

with $l_u = \alpha l_a$ then,

$$T = \frac{\alpha {B_{S1}}^2 A_{core} l_u}{18.64 \mu_0}$$

Appendix D. Analyzing Inductance Values for Rotor Blades

The simulation values of inductance need to be evaluated in order to determine the best rotor shape. The data obtained for Rotor 58 are in Table D-1. Values of current follow the characteristic current equation assuming I_{max} = 53 A. Thus the nominal torque is:

$$T = \frac{L_{max} I_{max}{}^2}{18.64} = \frac{10.45mH \times (53A)^2}{18.64} = 1.575\ Nm$$

Table D-1: Evaluating inductance values for Rotor 58 shape

Rotor angle, θ	Simulated L (mH)	Desired L (mH)	Percent error (%)	Current (A)	Energy (J)	Torque (N-m)
0°	2.215	2.242	1.25	53.000	3.110	-
5°	2.238	2.345	4.55	50.687	2.875	2.696
10°	2.331	2.457	5.12	48.375	2.727	1.691
15°	2.437	2.580	5.55	46.062	2.585	1.628
20°	2.557	2.717	5.88	43.750	2.447	1.584
25°	2.691	2.868	6.18	41.437	2.310	1.568
30°	2.874	3.038	5.39	39.125	2.200	1.267
35°	3.105	3.229	3.83	36.812	2.104	1.098
40°	3.366	3.445	2.29	34.500	2.003	1.154
45°	3.694	3.693	-0.04	32.187	1.913	1.027
50°	3.969	3.978	0.24	29.874	1.771	1.631
55°	4.200	4.312	2.60	27.562	1.595	2.015
60°	4.394	4.707	6.65	25.249	1.401	2.230
65°	4.824	5.182	6.90	22.937	1.269	1.509
70°	5.399	5.763	6.31	20.624	1.148	1.383
75°	6.322	6.491	2.60	18.312	1.060	1.012
80°	7.557	7.429	-1.73	15.999	0.967	1.063
85°	8.895	8.684	-2.43	13.686	0.833	1.536
90°	10.226	10.450	2.14	11.374	0.661	1.967

Using θ = 60° as an example for calculations:

Percent error:

$$\frac{L_{nominal}-L_{simulated}}{L_{nominal}} \times 100\% = \frac{4.394-4.707}{4.394} \times 100\% = 6.65\%$$

Energy (approximately):

$$W_n = \frac{1}{2} L_n {I_n}^2 = \frac{1}{2} 4.394mH \times (25.249A)^2 = 1.401\,J$$

Torque (approximately):

$$T = -\frac{\Delta W(\lambda,\theta)}{\Delta\theta}\Big|_{\lambda} = -\frac{W_n - W_{n-1}}{\theta_n - \theta_{n-1}} = -\frac{1.401-1.595}{(60°-55°) \times \frac{\pi}{180}} = 2.23\,Nm$$

Appendix E. Notes on Adding Motion to the Transient Simulation

Required for the motion setup is a disk ('air_rotor') that encapsulates the rotor and a motion band ('band'), a regular polyhedron that encapsulates the air_rotor. Both are given the material property of vacuum. Most errors encountered are due to some number of overlapping nodes between the moving and stationary portions of the mesh. Through many meshing failures, the specifications that allow simulation are in Table E-1. Success of the mesh seems to be dependent on having a sufficient number of sides for the band as well as sufficient clearances between the stator poles, band, air_rotor, and the rotor. Through trial-and-error it was determined the difference between the air_rotor and band thicknesses must be about 0.014 cm. Then the gap between these parts is centered upon the midway point of the rotor to stator pole gap (0.159 cm).

Table E-1: Specification of modeling rotor rotation

Model Part	Shape	Radius (cm)	Thickness (cm)
rotor	disk	10	0.144
air_rotor	disk	10.25	0.152
band	regular polyhedron (180 sides)	10.5	0.166

Appendix F. Simulation Data for Finalized AFVRM Model

The following data is collected using Rotor 58, a speed of 6000 rpm, and a simulation time step of 0.1 ms.

Table F-1: Simulation data for current, flux linkage, and induced voltage

Time (ms)	Position (deg)	Winding A Current (A)	Winding A Flux Linkage (Wb)	Winding A Induced Voltage (V)
0.0	0.0	53.000	0.119	23.868
0.1	3.6	51.335	0.128	16.880
0.2	7.2	49.670	0.118	-92.881
0.3	10.8	48.005	0.116	-28.290
0.4	14.4	46.340	0.110	-54.355
0.5	18.0	44.675	0.110	0.851
0.6	21.6	43.010	0.114	37.689
0.7	25.2	41.345	0.123	90.801
0.8	28.8	39.680	0.131	77.237
0.9	32.4	38.015	0.141	101.788
1.0	36.0	36.350	0.140	-13.737
1.1	39.6	34.685	0.136	-34.306
1.2	43.2	33.020	0.130	-66.478
1.3	46.8	31.354	0.128	-14.736
1.4	50.4	29.689	0.126	-22.132
1.5	54.0	28.024	0.124	-21.334
1.6	57.6	26.359	0.118	-56.920
1.7	61.2	24.694	0.113	-52.079
1.8	64.8	23.029	0.113	0.031
1.9	68.4	21.364	0.114	7.165
2.0	72.0	19.699	0.117	30.391
2.1	75.6	18.034	0.122	50.108
2.2	79.2	16.369	0.125	36.502
2.3	82.8	14.704	0.125	1.368
2.4	86.4	13.039	0.125	-4.888
2.5	90.0	11.374	0.120	-49.056

Table F-2: Simulation data for torque and losses

Time (ms)	Position (deg)	Torque1.Torque (N-m)	Moving1.Torque (N-m)	Solid Loss (W)	Stranded Loss (W)
0.0	0.0	0.077	0.021	0.000	72.574
0.1	3.6	1.581	-10.356	10.111	68.086
0.2	7.2	1.618	-3.994	8.128	63.741
0.3	10.8	1.472	-0.218	7.153	59.539
0.4	14.4	1.858	-0.842	6.291	55.480
0.5	18.0	1.532	-0.368	5.352	51.565
0.6	21.6	1.792	-1.962	4.270	47.793
0.7	25.2	1.920	0.395	2.429	44.164
0.8	28.8	1.820	-1.351	1.601	40.679
0.9	32.4	8.470	1.312	0.630	37.336
1.0	36.0	11.091	5.919	0.485	34.137
1.1	39.6	10.078	4.695	0.471	31.081
1.2	43.2	12.231	7.410	0.607	28.169
1.3	46.8	9.016	3.178	0.804	25.400
1.4	50.4	7.804	5.356	1.672	22.774
1.5	54.0	7.376	5.940	2.403	20.291
1.6	57.6	7.355	4.467	3.909	17.951
1.7	61.2	7.035	5.087	4.659	15.755
1.8	64.8	7.103	5.377	5.086	13.702
1.9	68.4	5.400	3.246	4.738	11.792
2.0	72.0	5.200	3.059	4.122	10.026
2.1	75.6	4.580	3.635	3.385	8.403
2.2	79.2	3.880	2.453	2.599	6.923
2.3	82.8	3.291	2.540	1.911	5.586
2.4	86.4	2.571	1.517	1.276	4.393
2.5	90.0	0.996	1.210	0.853	3.342